

Black hole jets on the scale of the Cosmic Web

Martijn S.S.L. Oei^{1,2}, Martin J. Hardcastle³, Roland Timmerman^{1,4}, Aivin R.D.J.G.I.B. Gast⁵, Andrea Botteon⁶, Antonio C. Rodriguez², Daniel Stern⁷, Gabriela Calistro Rivera⁸, Reinout J. van Weeren¹, Huub J.A. Röttgering¹, Huib T. Intema¹, Francesco de Gasperin⁶, and S.G. Djorgovski²

¹*Leiden Observatory, Leiden University, Niels Bohrweg 2, Leiden, 2333 CA, Zuid-Holland, the Netherlands*

²*Cabill Center for Astronomy and Astrophysics, California Institute of Technology, 1216 E California Blvd, Pasadena, CA 91125, California, the United States*

³*Centre for Astrophysics Research, University of Hertfordshire, College Lane, Hatfield, AL10 9AB, Hertfordshire, the United Kingdom*

⁴*Centre for Extragalactic Astronomy, Department of Physics, Durham University, Durham, DH1 3LE, the United Kingdom*

⁵*Somerville College, University of Oxford, Woodstock Road, Oxford, OX2 6HD, Oxfordshire, the United Kingdom*

⁶*INAF-IRA, Via P. Gobetti 101, 40129, Bologna, Italy*

⁷*Jet Propulsion Laboratory, California Institute of Technology, 4800 Oak Grove Drive, Mail Stop 264-789, Pasadena, CA 91109, the United States*

⁸*European Southern Observatory, Karl-Schwarzschild-Strasse 2, 85748, Garching bei München, Germany*

Summary Paragraph

When sustained for megayears [1, 2], high-power jets from supermassive black holes become the Universe’s largest galaxy-made structures [3]. By pumping electrons, atomic nuclei, and magnetic fields into the intergalactic medium, these energetic flows affect the distribution of matter and magnetism in the Cosmic Web [4–6], and could have a sweeping cosmological influence if they reached far at early epochs. For the last fifty years, the known size range of black hole jet pairs terminated at 4.6–5.0 Mpc [7–9], or 20–30% of a cosmic void radius in the Local Universe [10]. An observational lack of longer jets, as well as theoretical results [11], thus suggested a growth limit at ~ 5 Mpc [12]. Here we report observations of a radio structure spanning ~ 7 Mpc, or $\sim 66\%$ of a coeval cosmic void radius, apparently generated by a black hole between $4.4_{-0.7}^{+0.2}$ –6.3 Gyr after the Big Bang. The structure consists of a northern lobe, a northern jet, a core, a southern jet with an inner hotspot, and a southern outer hotspot with a backflow. This system demonstrates that jets can avoid destruction by magnetohydrodynamical instabilities over cosmological distances, even at epochs when the Universe was $7\text{--}15_{-2}^{+6}$ times denser than it is today. How jets can retain such long-lived coherence is presently unknown.

Keywords: Active galactic nuclei, astrophysical jets, giant radio galaxies, intergalactic medium

Main Text

To quantify the impact of black hole energy transport on the intergalactic medium (IGM), radio images from the International LOFAR Telescope (ILT) have recently been searched [e.g. 9, 13–15] for Mpc-scale galactic outflows. In particular, our team systematically scanned the ILT’s ongoing northern sky survey at wavelength $\lambda = 2.08$ m both with machine learning and by eye — the latter with significant contributions from citizen scientists [16]. This endeavour has increased the number of known Mpc-scale outflows from a few hundred to over eleven thousand [15]. Our largest find is the outflow shown in Fig. 1 and Extended Data Fig. 1, which we name Porphyryon. The

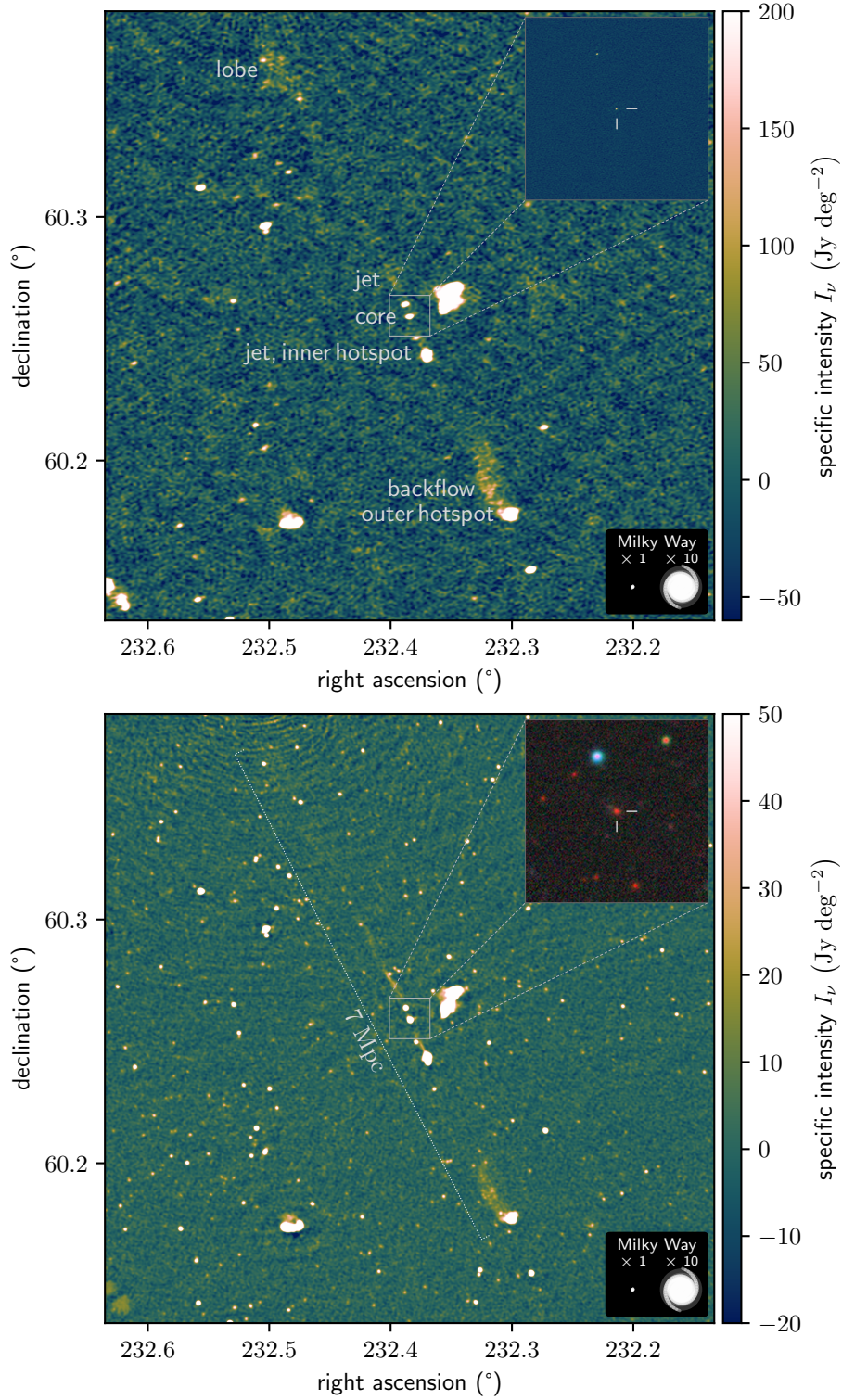


Figure 1: **Deep radio images of a 7 Mpc-long, black hole-driven outflow at central wavelengths $\lambda = 2.08$ m and $\lambda = 0.46$ m.** These images, (a) and (b), were taken with the ILT and uGMRT, respectively, and have resolutions of $6.2''$ and $4.3''$. Panel (a)'s inset shows ILT VLBI imagery at $\lambda = 2.08$ m and a resolution of $0.4''$. Panel (b)'s inset shows Legacy DR10 optical-infrared imagery. The larger images cover $15' \times 15'$ of sky, whilst the insets cover $1' \times 1'$. For scale, we show the stellar Milky Way disk (diameter: 50 kpc) and a ten times inflated version.

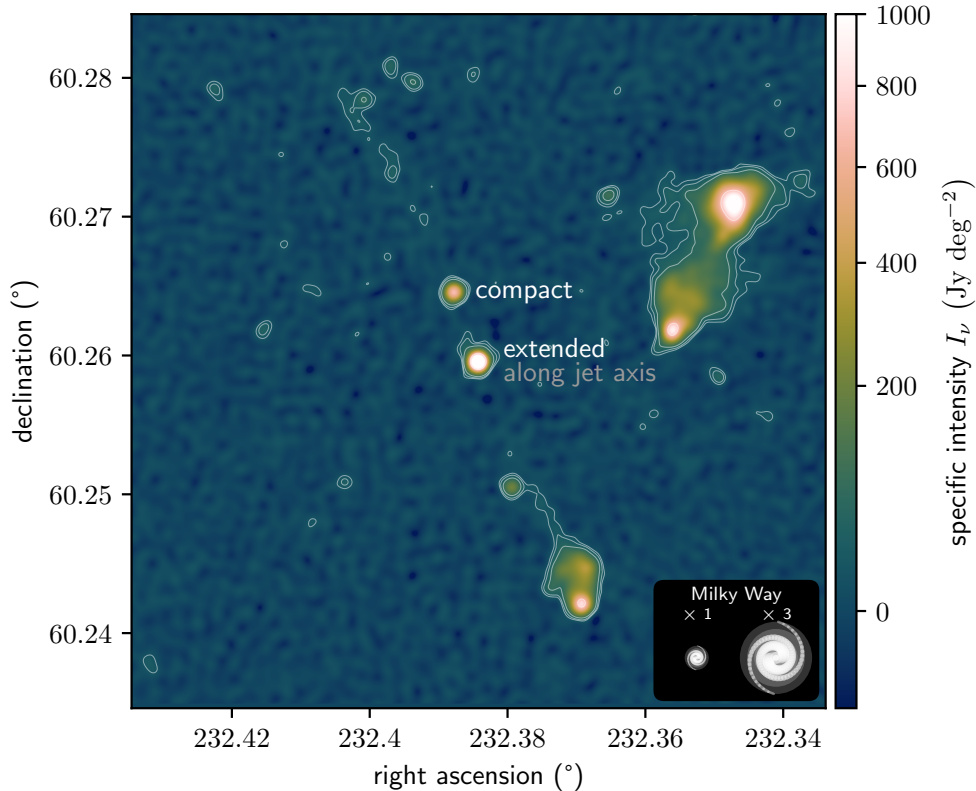


Figure 2: **In our imagery, only the southern host galaxy candidate features a radio extension along Porphyrion’s overarching jet axis.** For the central $3' \times 3'$ sky area, we show a uGMRT image at $\lambda = 0.46$ m and $3.6''$ resolution. We detect the southern galaxy’s radio extension, directed towards the north-northeast, at 5 s.d. (σ) significance. The contours denote 3σ , 5σ , 10σ , and 100σ .

source, of angular length $\phi = 13.4' \pm 0.1'$, appears unusually thin. To investigate from which galaxy along the jet axis the outflow originates, we processed ILT very-long-baseline interferometry (VLBI) data of the central $4' \times 4'$. At a spatial resolution of 3 kpc, the image (Fig. 1’s top panel inset and Extended Data Fig. 2) shows lone, unresolved radio sources in two galaxies, in both cases implying active accretion onto a supermassive black hole (SMBH). Because the detection of jets near either black hole (and along the overarching NNE–SSW axis) would clarify Porphyrion’s origin, we performed deep follow-up observations with the Upgraded Giant Metrewave Radio Telescope (uGMRT) at $\lambda = 0.46$ m. The resulting image and ancillary DESI Legacy Imaging Surveys (Legacy) optical–infrared data (Fig. 1’s bottom panel) reveal that the outflow protrudes from a massive ($M_{\star} = 6.7_{-1.4}^{+1.4} \cdot 10^{11} M_{\odot}$) galaxy. This is visually clear in Fig. 2, which is processed to highlight the radio morphologies of the two central galaxies. Of these, the southernmost galaxy uniquely displays a 5σ extension along Porphyrion’s overarching jet axis. We observed this galaxy with the Low Resolution Imaging Spectrometer (LRIS) on the W. M. Keck Observatory’s Keck I Telescope, measuring a spectroscopic redshift $z = 0.896 \pm 0.001$ (Fig. 3’s top panel). We witness Porphyrion at $t_{\text{BB}} = 6.3$ Gyr after the Big Bang.

The outflow’s angular length and redshift entail a sky-projected length $l_{\text{p}} = 6.43 \pm 0.05$ Mpc. This makes Porphyrion the projectively longest known structure generated by an astrophysical body. The outflow’s total length exceeds this projected length, but by how much depends on the

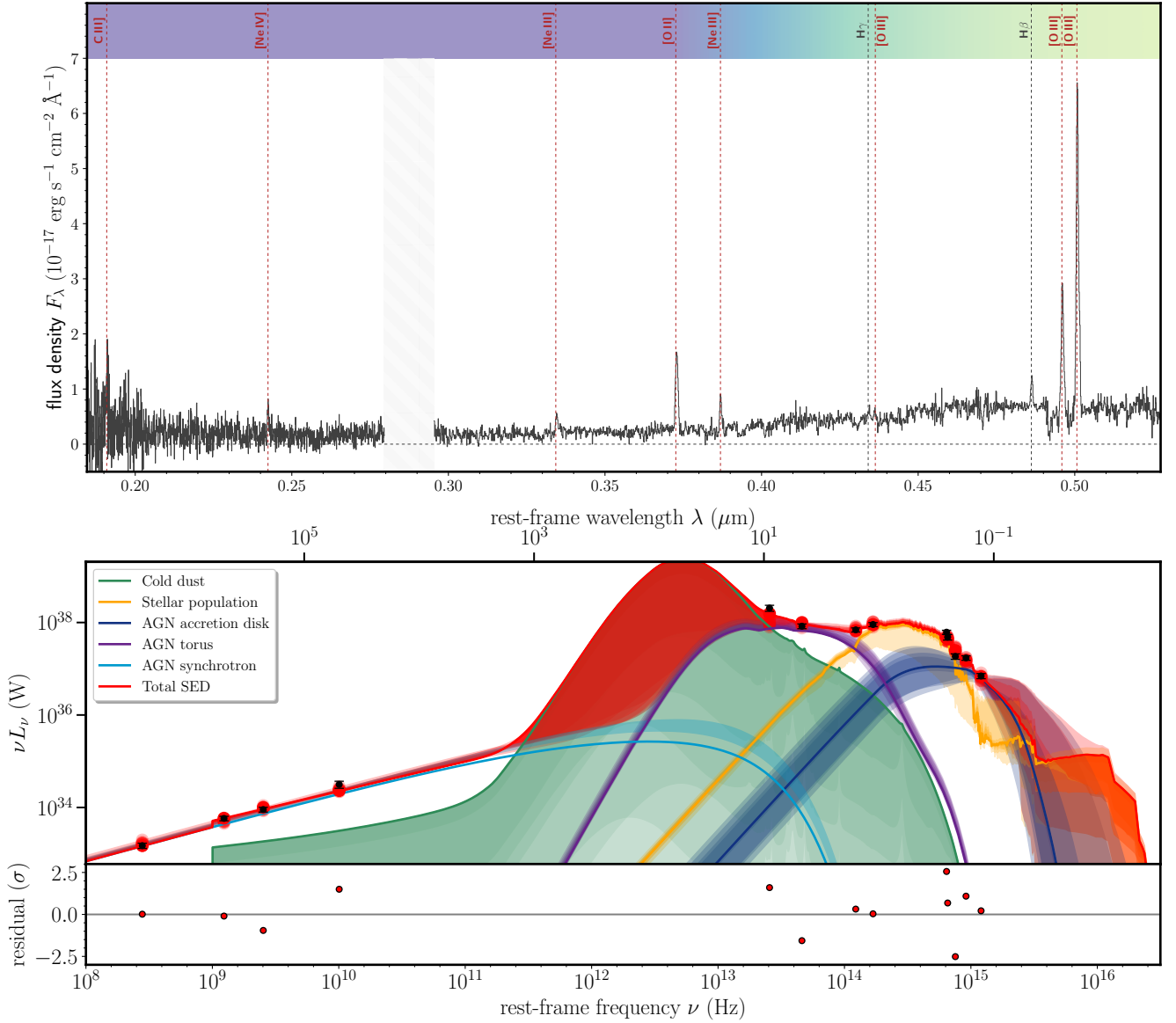


Figure 3: **Both rest-frame ultraviolet–optical spectroscopy and radio–ultraviolet photometry demonstrate that the outflow’s host galaxy harbours an RE AGN.** **a)** LRIS spectrum exhibiting hydrogen, carbon, oxygen, and neon emission. The forbidden lines from multiply ionised oxygen and neon (dark red) could not be generated by even the hottest stars, and instead stem from the narrow-line region of an RE AGN at a redshift $z = 0.896 \pm 0.001$. **b)** Bayesian inference of the galaxy’s SED (Methods) favours the presence of an AGN accretion disk (dark blue) with an obscuring torus (purple), again indicating radiative efficiency.

56 unknown inclination of the jets with respect to the sky plane. Deprojection formulae [14] predict
 57 a total length $l = 6.8^{+1.2}_{-0.3}$ Mpc, with expectation $\mathbb{E}[L | L_p = l_p] = 7.28 \pm 0.05$ Mpc (Meth-
 58 ods). We thus estimate Porphyryon to be ~ 7 Mpc long in total. Spanning $\sim 66\%$ of the radius
 59 of a typical cosmic void at its redshift, the outflow is truly cosmological. Surprisingly, SMBH jets
 60 can remain collimated over several megaparsecs, despite the growth of (magneto)hydrodynamical
 61 (MHD) instabilities — chiefly Kelvin–Helmholtz instabilities — predicted theoretically and seen

in simulations of shorter jets [e.g. [II](#)]. Similarly, prolonged entrainment of mass from the IGM, even at $z \gtrsim 1$, does not necessarily destabilise jets. No MHD simulations of Mpc-scale jets yet exist: the spatio-temporal grids required imply a numerical cost $\sim 10^2$ times higher than that of state-of-the-art runs. Outflows like Porphyrion thus offer a window into a jet physics regime that, at present, cannot be explored numerically.

Active galactic nuclei (AGN) with accretion disks extending to the innermost stable circular orbits of their SMBHs efficiently convert the gravitational potential energy of infalling matter into radiation, and are thus called radiatively efficient (RE); all others are called radiatively inefficient (RI) [[17](#), [18](#)]. In RE AGN, the luminous accretion disk photo-ionises a circumnuclear region emitting narrow, and often forbidden, spectral lines. The Keck-observed prominence of forbidden ultraviolet–optical lines from oxygen and neon (chiefly that of the [O III] $\lambda 5007$ line, which is 10.3 ± 0.2 times brighter than the $H\beta$ line) therefore reveals the presence of an RE AGN [[19](#)]. Bayesian inference of the galaxy’s spectral energy distribution (SED; Methods and Fig. 3’s bottom panel) independently suggests the presence of a luminous SMBH accretion disk with an obscuring torus: our model requires these structures to explain the observed infrared (WISE) and near-ultraviolet (Legacy) flux levels, which exceed those possible with cold dust and stars alone.

By contrast, all previous record-length outflows, such as 3C 236 ($l_p = 4.6$ Mpc; [[7](#)]), J1420–0545 ($l_p = 4.9$ Mpc; [[8](#)]), and Alcyoneus ($l_p = 5.0$ Mpc; [[9](#)]), are fuelled by RI AGN in recent history ($t_{\text{BB}} = 10.2\text{--}12.4$ Gyr). Whereas RI AGN occur primarily in evolved, ‘red and dead’ ellipticals [[17](#)], RE AGN feature vigorous gas inflows and are thus generally found in star-forming galaxies. Indeed, in the first billions of years of cosmic time, RE AGN dominated the radio-luminous AGN population [[20](#)]. The potential of Mpc-scale outflows to spread cosmic rays, heat, heavy atoms, and magnetic fields through the IGM is particularly high if large specimina could emerge from the type of AGN abundant at early epochs, when the Universe was smaller. The discovery of a 7 Mpc–long, RE AGN–fuelled outflow before cosmic half-time therefore highlights the hitherto understudied cosmological transport capabilities of Mpc-scale outflows.

In the Local Universe, $\sim 30\%$ of all luminous Mpc-scale outflows reside in galaxy clusters, $\sim 60\%$ in galaxy groups, and the remaining $\sim 10\%$ in more dilute parts of filaments, in sheets, or in voids [[21](#)]. The Legacy DR10 (shown in Fig. 1’s bottom panel inset) suggests that Porphyrion does not originate from a galaxy cluster: the closest known cluster [[22](#)] lies at a comoving distance of 30^{+12}_{-17} Mpc, or 31^{+14}_{-16} cluster radii (Methods). The nearest *Planck* Sunyaev–Zel’dovich detection [[23](#)] is $\sim 2^\circ$ away. Concordantly, studies have found that jet-fuelling RE AGN avoid rich environments [[24](#), [25](#)]. In a sphere with a comoving radius of 10 Mpc centred around Porphyrion’s host, we counted 35 ± 6 other Legacy-detected galaxies. By also performing galactic neighbour counts for a control sample of galaxies at comparable redshifts, and by assuming that galactic neighbour counts increase with circumgalactic Cosmic Web density, we estimated Porphyrion’s circumgalactic Cosmic Web density percentile to be $42^{+26}_{-23}\%$ (Methods). This suggests that Porphyrion does not originate from a void. The straightness of the outflow implies a low peculiar speed ($v_p \lesssim 10^2$ km s $^{-1}$), consistent with the host being at the bottom of a local gravitational potential well. The evidence implies that Porphyrion originates from a Cosmic Web filament, and from a galaxy group in particular. Vast voids, which make up the bulk ($\sim 80\%$) of the Universe’s volume [[26](#)], surround such structures in most directions. Jets as long as Porphyrion’s thus encounter void-like densities and temperatures with considerable probability. Indeed, the collimated nature of the jets favours scenarios in which they descend into voids, as jets gain resilience against Kelvin–Helmholtz instabilities when the ambient density declines [e.g. [II](#)]. Dynamical modelling

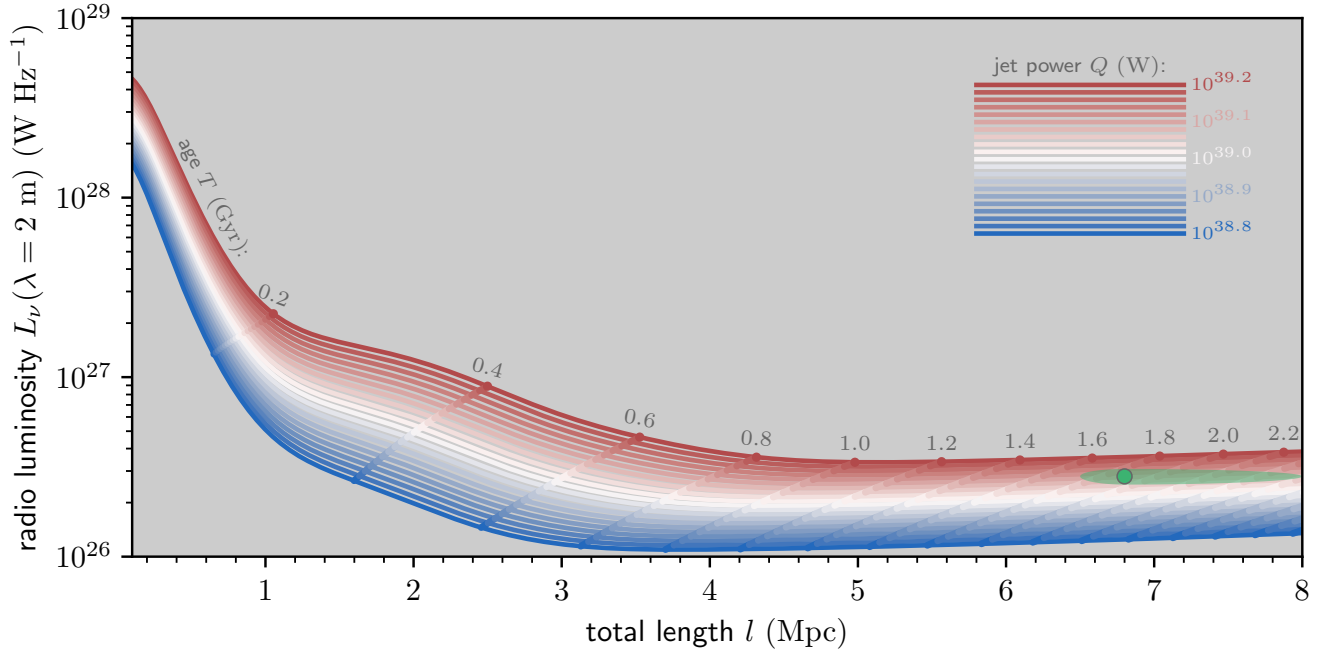


Figure 4: **By superimposing Porphyrion’s total length and radio luminosity on evolutionary tracks from dynamical modelling, we inferred the outflow’s two-sided jet power and age.** We assumed the host galaxy to reside in a galaxy group bordering voids, through which the jets eventually travel. The width and height of Porphyrion’s uncertainty ellipse both cover 68% of probability centred around the median (green dot).

107 suggests a two-sided jet power $Q = 1.3 \pm 0.1 \cdot 10^{39}$ W and an age $T = 1.9_{-0.2}^{+0.7}$ Gyr (Fig. 4; Meth-
 108 ods). The outflow’s average expansion speed $v = 0.012 c$, comparable to Alcyoneus’ [9]. In voids
 109 and the warm-hot IGM, the speed of sound $c_s \sim 10^0 - 10^1$ km s $^{-1}$: the jets grow hypersonically at
 110 Mach numbers $\mathcal{M} \sim 10^2 - 10^3$ and drive strong shocks into voids. Porphyrion’s jets have carried
 111 an energy $E = QT = 8_{-1}^{+2} \cdot 10^{55}$ J into the IGM — an amount comparable to the energy released
 112 during galaxy cluster mergers [e.g. 27]. This suggests that the outflow is among the most energetic
 113 post-Big Bang events to have occurred in its Cosmic Web region. Even though the SMBH might
 114 have gained a significant fraction of its mass while powering the jets ($\Delta M_\bullet > 2 \frac{E}{c^2} = 9_{-1}^{+2} \cdot 10^8 M_\odot$),
 115 it appears to have maintained a constant spin axis throughout gigayears of activity. Shocks running
 116 perpendicular to the jets dissipate enough heat into the filament to increase its temperature by
 117 $\Delta T \sim 10^7$ K and its radius by $\Delta r \sim 1$ Mpc (Methods). Outflows like Porphyrion thus locally
 118 alter the Cosmic Web’s shape.

119 Figure 4 illustrates that the radio luminosities of Mpc-long outflows with constant jet power ini-
 120 tially decrease before stabilising to a jet power-dependent level. Active outflows not only lengthen,
 121 but also grow volumetrically [15]; consequently, the mean radio luminosity per unit of lobal vol-
 122 ume drops over time. In turn, lobal radio surface brightnesses decrease [21], impeding outflow de-
 123 tection [14, 15]. As Fig. 1 evinces, Porphyrion borders on the noise of leading current-day telescopes;
 124 thus, outflows further progressed on the same evolutionary track hitherto evade detection. Similar
 125 outflows are likewise undetectable at lower jet powers and at higher redshifts, where increased in-
 126 verse Compton scattering with the CMB diverts electron energy away from synchrotron radiation
 127 — causing lower radio luminosities at fixed jet powers [28]. Problematically, cosmological surface
 128 brightness dimming further reduces radio surface brightnesses by a factor of $(1 + z)^{3-\alpha}$, where α

is the radio spectral index. Statistical modelling [14, 15] indeed suggests that the detectable population is just the tip of the iceberg: owing to their apparent faintness, most Mpc-scale outflows are still concealed by noise. These arguments, and the fact that our search covered only $\sim 15\%$ of the sky, imply the existence of a hidden population of outflows with sizes comparable to, and possibly larger than, Porphyrior's.

Porphyrior indicates that RE AGN may be at least as effective at generating Mpc-scale outflows as RI AGN are in the Local Universe. If the comoving number density of actively powered Mpc-scale outflows has remained roughly constant over time at $\sim 10^1 (100 \text{ Mpc})^{-3}$ [14, 15], and a comoving volume of $(100 \text{ Mpc})^3$ contains $\sim 10^2$ filaments, then there would exist $\sim 10^{-1}$ actively powered Mpc-scale outflows in every filament at every instant. As their jets endure for $\sim 10^{-2} - 10^0$ Gyr [1, 3, 9], $\sim 10^1$ Mpc-scale outflows may have been generated in every filament throughout cosmic history. If jet powers $Q \sim 10^{38}$ W are typical [1, 9, 28], Mpc-scale outflows induce significant heating ($\Delta T \sim 10^6$ K) and expansion ($\Delta r \sim 10^{-1}$ Mpc) of cosmic filaments (Methods), which comprise the Universe's primary baryon reservoir. Whereas AGN feedback has been known to maintain the thermodynamic state in the $\sim 1 \text{ Mpc}^3$ -scale volumes of galaxy clusters, Porphyrior's discovery highlights the importance of black hole energy transport in the Cosmic Web at large.

References

1. Hardcastle, M. J. *et al.* Radio-loud AGN in the first LoTSS data release. The lifetimes and environmental impact of jet-driven sources. *A&A* **622**, A12 (2019).
2. Perucho, M., Martí, J.-M. & Quilis, V. Long-term FR II jet evolution: clues from three-dimensional simulations. *MNRAS* **482**, 3718–3735 (2019).
3. Dabhade, P., Saikia, D. J. & Mahato, M. Decoding the giant extragalactic radio sources. *Journal of Astrophysics and Astronomy* **44**, 13 (2023).
4. Ayromlou, M., Nelson, D. & Pillepich, A. Feedback reshapes the baryon distribution within haloes, in halo outskirts, and beyond: the closure radius from dwarfs to massive clusters. *MNRAS* **524**, 5391–5410 (2023).
5. Beck, A. M., Hanasz, M., Lesch, H., Remus, R. -. & Staszczyn, F. A. On the magnetic fields in voids. *MNRAS* **429**, L60–L64 (2013).
6. Vazza, F. *et al.* Simulations of extragalactic magnetic fields and of their observables. *Classical and Quantum Gravity* **34**, 234001 (2017).
7. Willis, A. G., Strom, R. G. & Wilson, A. S. 3C236, DA240; the largest radio sources known. *Nature* **250**, 625–630 (1974).
8. Machalski, J., Koziel-Wierzbowska, D., Jamroz, M. & Saikia, D. J. J1420-0545: The Radio Galaxy Larger than 3C 236. *ApJ* **679**, 149–155 (2008).
9. Oei, M. S. S. L. *et al.* The discovery of a radio galaxy of at least 5 Mpc. *A&A* **660**, A2 (2022).
10. Correa, C. M. *et al.* Redshift-space effects in voids and their impact on cosmological tests. Part I: the void size function. *MNRAS* **500**, 911–925 (2021).
11. Perucho, M. Dissipative Processes and Their Role in the Evolution of Radio Galaxies. *Galaxies* **7**, 70 (2019).
12. Andernach, H., Jiménez-Andrade, E. F. & Willis, A. G. Discovery of 178 Giant Radio Galaxies in 1059 deg² of the Rapid ASKAP Continuum Survey at 888 MHz. *Galaxies* **9**, 99 (2021).
13. Dabhade, P. *et al.* Giant radio galaxies in the LOFAR Two-metre Sky Survey. I. Radio and environmental properties. *A&A* **635**, A5 (2020).

171 14. Oei, M. S. S. L. *et al.* Measuring the giant radio galaxy length distribution with the LoTSS. *A&A* **672**, A163
172 (2023).

173 15. Mostert, R. I. J. *et al.* Constraining the giant radio galaxy population with machine learning and Bayesian infer-
174 ence. *arXiv e-prints*, arXiv:2405.00232 (2024).

175 16. Hardcastle, M. J. *et al.* The LOFAR Two-Metre Sky Survey. VI. Optical identifications for the second data re-
176 lease. *A&A* **678**, A151 (2023).

177 17. Heckman, T. M. & Best, P. N. The Coevolution of Galaxies and Supermassive Black Holes: Insights from Sur-
178 veys of the Contemporary Universe. *ARA&A* **52**, 589–660 (2014).

179 18. Hardcastle, M. Interpreting radiative efficiency in radio-loud AGNs. *Nature Astronomy* **2**, 273–274 (2018).

180 19. Buttiglione, S. *et al.* An optical spectroscopic survey of the 3CR sample of radio galaxies with $z < 0.3$. II.
181 Spectroscopic classes and accretion modes in radio-loud AGN. *A&A* **509**, A6 (2010).

182 20. Williams, W. L. *et al.* LOFAR-Boötes: properties of high- and low-excitation radio galaxies at $0.5 < z < 2.0$.
183 *MNRAS* **475**, 3429–3452 (2018).

184 21. Oei, M. S. S. L. *et al.* Luminous giants populate the dense Cosmic Web: The radio luminosity-environmental
185 density relation for radio galaxies in action. *arXiv e-prints*, arXiv:2404.17776 (2024).

186 22. Wen, Z. L. & Han, J. L. A catalog of 1.58 million clusters of galaxies identified from the DESI Legacy Imaging
187 Surveys. *arXiv e-prints*, arXiv:2404.02002 (2024).

188 23. Planck Collaboration *et al.* Planck 2015 results. XXVII. The second Planck catalogue of Sunyaev-Zeldovich
189 sources. *A&A* **594**, A27 (2016).

190 24. Ineson, J. *et al.* Radio-loud Active Galactic Nucleus: Is There a Link between Luminosity and Cluster Environ-
191 ment? *ApJ* **770**, 136 (2013).

192 25. Ineson, J. *et al.* The link between accretion mode and environment in radio-loud active galaxies. *MNRAS* **453**,
193 2682–2706 (2015).

194 26. Forero-Romero, J. E., Hoffman, Y., Gottlöber, S., Klypin, A. & Yepes, G. A dynamical classification of the cos-
195 mic web. *MNRAS* **396**, 1815–1824 (2009).

196 27. van Weeren, R. J. *et al.* Radio observations of ZwCl 2341.1+0000: a double radio relic cluster. *A&A* **506**, 1083–
197 1094 (2009).

198 28. Hardcastle, M. J. A simulation-based analytic model of radio galaxies. *MNRAS* **475**, 2768–2786 (2018).

199 List of Figures

200 1 **Deep radio images of a 7 Mpc–long, black hole–driven outflow at central wavelengths**
201 $\lambda = 2.08$ m and $\lambda = 0.46$ m. These images, (a) and (b), were taken with the ILT and
202 uGMRT, respectively, and have resolutions of $6.2''$ and $4.3''$. Panel (a)’s inset shows ILT VLBI
203 imagery at $\lambda = 2.08$ m and a resolution of $0.4''$. Panel (b)’s inset shows Legacy DR10 optical–
204 infrared imagery. The larger images cover $15' \times 15'$ of sky, whilst the insets cover $1' \times 1'$. For
205 scale, we show the stellar Milky Way disk (diameter: 50 kpc) and a ten times inflated version. 2

206 2 **In our imagery, only the southern host galaxy candidate features a radio extension**
207 **along Porphyrion’s overarching jet axis.** For the central $3' \times 3'$ sky area, we show a uGMRT
208 image at $\lambda = 0.46$ m and $3.6''$ resolution. We detect the southern galaxy’s radio extension,
209 directed towards the north-northeast, at 5 s.d. (σ) significance. The contours denote 3σ , 5σ ,
210 10σ , and 100σ 3

211	3	Both rest-frame ultraviolet–optical spectroscopy and radio–ultraviolet photometry demonstrate that the outflow’s host galaxy harbours an RE AGN. a) LRIS spectrum exhibiting hydrogen, carbon, oxygen, and neon emission. The forbidden lines from multiply ionised oxygen and neon (dark red) could not be generated by even the hottest stars, and instead stem from the narrow-line region of an RE AGN at a redshift $z = 0.896 \pm 0.001$. b) Bayesian inference of the galaxy’s SED (Methods) favours the presence of an AGN accretion disk (dark blue) with an obscuring torus (purple), again indicating radiative efficiency.	4
212			
213			
214			
215			
216			
217			
218	4	By superimposing Porphyrior’s total length and radio luminosity on evolutionary tracks from dynamical modelling, we inferred the outflow’s two-sided jet power and age. We assumed the host galaxy to reside in a galaxy group bordering voids, through which the jets eventually travel. The width and height of Porphyrior’s uncertainty ellipse both cover 68% of probability centred around the median (green dot).	6
219			
220			
221			
222			

223 Methods

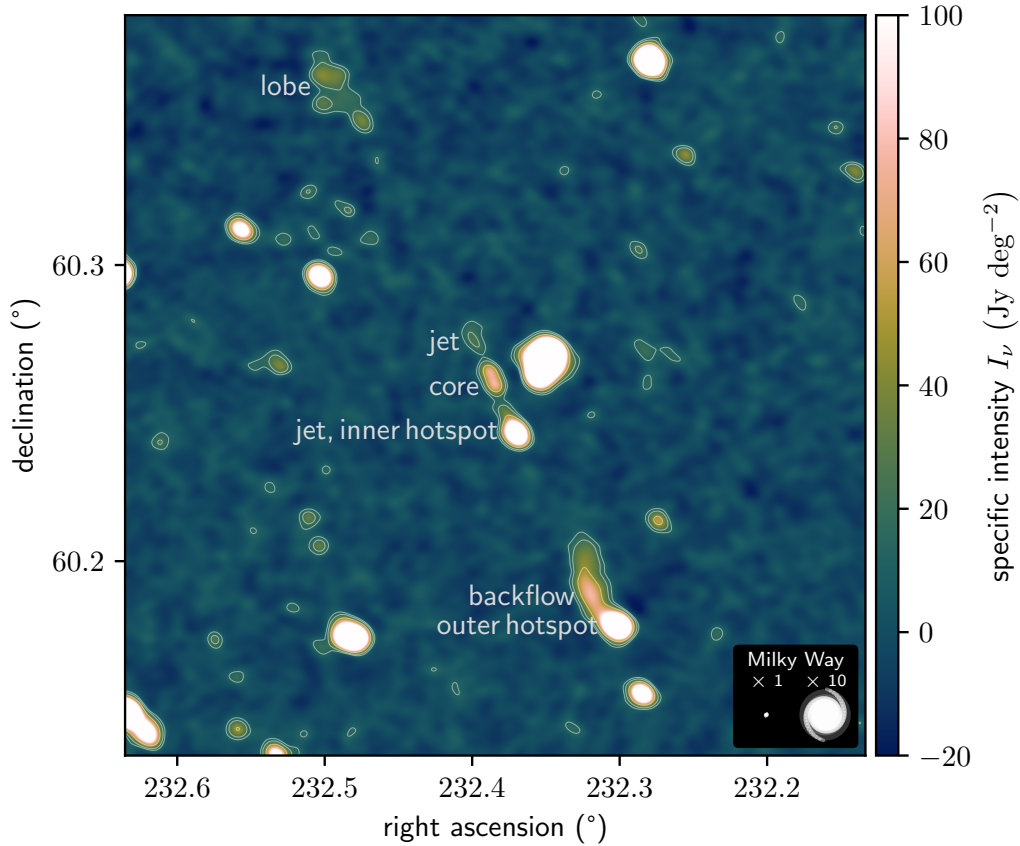
224 Throughout this work, we assume a flat, inflationary Λ CDM cosmological model with parameters from Planck
225 Collaboration *et al.* [1]: $h = 0.6766$, $\Omega_{\text{BM},0} = 0.0490$, $\Omega_{\text{M},0} = 0.3111$, and $\Omega_{\Lambda,0} = 0.6889$. We define
226 $\Omega_{\text{DM},0} := \Omega_{\text{M},0} - \Omega_{\text{BM},0} = 0.2621$ and $H_0 := h \cdot 100 \text{ km s}^{-1} \text{ Mpc}^{-1}$. Furthermore, we define the spectral in-
227 dex α so that it relates to flux density F_ν at frequency ν as $F_\nu \propto \nu^\alpha$. Under this convention, synchrotron spectral
228 indices are *positive* (i.e. $\alpha = \frac{5}{2}$) for the lowest frequencies and *negative* for higher frequencies. As the restoring
229 PSFs may not be perfectly circular, all reported resolutions are effective resolutions. In other works, Mpc-scale
230 outflows are usually called ‘giant radio galaxies’. (Although Mpc-scale outflows are generated by galaxies, they
231 are not galaxies themselves; therefore, referring to them as a class of ‘galaxies’ could cause confusion. In addition,
232 Mpc-scale outflows may have been primarily studied through radio observations, but their synchrotron losses
233 (like their other radiative losses) appear to have only a minor effect on their evolution [2], suggesting that ‘radio’
234 should not be used in a name meant to describe these objects intrinsically. Finally, while ‘giant’ appears apt, it is
235 also vague; we thus prefer the more quantitative ‘Mpc-scale’.)

236 **ILT observations and data reduction** The International LOFAR Telescope [ILT; 3] is exquisitely sensitive
237 to the metre-wavelength synchrotron radiation generated by electrons and positrons in the first tens to hundreds
238 of megayears after their acceleration to relativistic energies. Consequently, the second data release [DR2; 4] of
239 the LOFAR Two-metre Sky Survey [LoTSS; 5], the ILT’s ongoing northern sky survey in the 120–168 MHz
240 frequency band, has revealed millions of galaxies boasting supermassive black hole (SMBH) jets.

241 After discovering Porphyryon, the outflow presented in this work, we extracted a total of 16 hours of DDFacet-
242 calibrated visibilities [6] from LoTSS pointings P228+60 and P233+60 (Project ID: LT5_007). (Porphyryon was
243 the son of Ouranos, the Greek primordial sky deity. According to Ps.-Apollodorus, he and Alcyoneus were the
244 greatest of the *Gigantes* (Giants), while Pindar called him the ‘King of the Giants’. He was struck by Zeus’s
245 thunderbolt in the Gigantomachy — the battle between the Giants and the Olympian gods for supremacy over
246 the Cosmos.) Following van Weeren *et al.* [7], we subtracted all sources far away from the target, performed
247 phase shifting and averaging, and self-calibrated the resulting data. This removed residual ionospheric artefacts
248 around ILTJ153004.28+602423.2, the brightest source in the arcminute-scale vicinity of the northern lobe. We
249 subsequently performed joint deconvolution on the recalibrated target visibilities with WSClean [8] using Briggs
250 weighting -0.5 , yielding the $6.2''$ -resolution image of Fig. 1’s top panel. The noise level is $\sigma = 25 \text{ Jy deg}^{-2}$ at
251 its lowest. The outflow appears thin: its width is nowhere more than a few percent of its length. We defined Por-
252 phryon’s angular length as the largest possible great-circle distance between a point in the southern hotspot and
253 a point in the northern lobe. The arc connecting these points defines the overarching jet axis, and we measured
254 its position angle to be $27 \pm 1^\circ$.

255 To investigate the presence of diffuse structure, we applied Gaussian tapering to the weights of the recal-
256 ibrated target visibilities. The taper’s FWHM in the (u, v) -plane was chosen such that the FWHM of the cor-
257 responding Gaussian in the sky plane equals $15''$. Again performing deconvolution with WSClean using Briggs
258 weighting -0.5 (albeit in multi-scale mode this time), we obtained the $19.8''$ -resolution image of Extended Data
259 Fig. 1. This image reveals the northern lobe more clearly. The noise level is $\sigma = 4.8 \text{ Jy deg}^{-2}$.

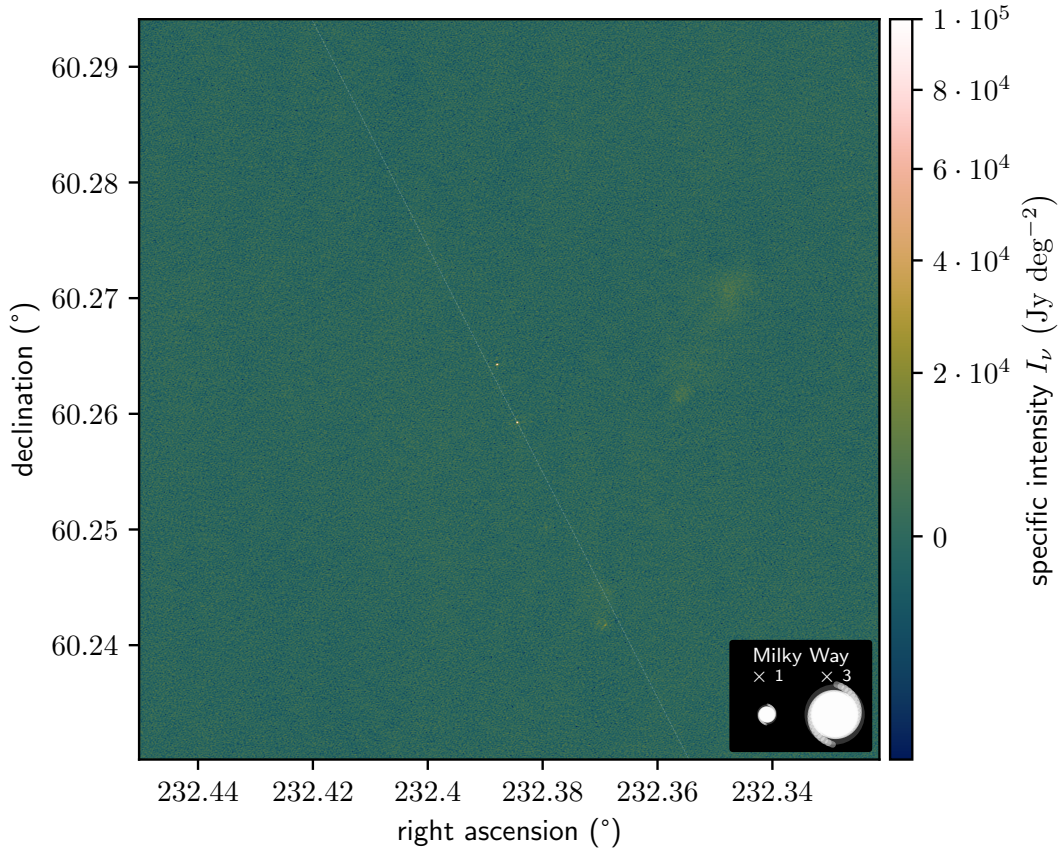
260 To obtain a high-resolution image of Porphyryon, we reprocessed the P233+60 data, including LOFAR’s
261 international stations, from scratch using the LOFAR-VLBI pipeline [9]. This pipeline builds upon the cali-
262 bration pipeline for the Dutch part of the array to calibrate the international stations. We derived the dispersive
263 phase corrections and gain corrections for the international stations by calibrating against a bright and compact
264 radio source near the target. In this case, we used the aforementioned ILTJ153004.28+602423.2, a known source
265 from the Long-Baseline Calibrator Survey [LBCS; 10, 11]. To reduce interference from unrelated radio sources



Extended Data Figure 1: **ILT image at central wavelength $\lambda = 2.08$ m, with a resolution of $19.8''$, highlighting diffuse emission in the northern lobe and southern backflow.** We show the same sky region and annotations as in Fig. 1. The contours denote 3σ , 5σ , and 10σ .

266 in Porphyrior’s angular vicinity, we phased up LOFAR’s core stations to narrow down the field of view and only
 267 considered data from long baselines to calculate the calibration solutions. With the calibration solutions applied
 268 in the direction of the target, we again performed deconvolution with WSClean (but using Briggs weighting o)
 269 to obtain a $0.4''$ -resolution image, which we show partially in Fig. 1’s top panel inset and fully in Extended Data
 270 Fig. 2. The noise level is $\sigma = 2.7 \cdot 10^3$ Jy deg $^{-2}$ at its lowest. This image, which covers the central one-third of
 271 the total jet system, reveals synchrotron emission at 42σ significance from active galactic nuclei (AGN) in only
 272 two galaxies, $19''$ apart. Both lie along the outflow’s jet axis nearly halfway between its endpoints. We considered
 273 these galaxies, J152933.03+601552.5 and J152932.16+601534.4, to be Porphyrior’s host candidates. In contrast to
 274 other radio-emitting structures along Porphyrior’s axis, such as the southern complex interpreted as an inner
 275 hotspot, these candidates have optical counterparts in Legacy Surveys DR10 imagery (see Fig. 1’s bottom panel
 276 inset).

277 **uGMRT observations and data reduction** On 13 May 2023, we observed the outflow with the Upgraded
 278 Giant Metrewave Radio Telescope [uGMRT; 12] in Band 4 (550–750 MHz) for a total of 10 hours. On 23 September
 279 2023, we extended these observations with another 5 hours. These observations are part of GMRT Observing
 280 Cycle 44 and have project code 44_101. We requested to record both narrow-band (GSB) and wide-band
 281 (GWB) data. Adverse ionospheric conditions during the September run prohibited us from improving upon
 282 the images produced with the May run data only. In what follows, we therefore exclusively discuss May run



Extended Data Figure 2: **Our ILT VLBI image of Porphyrior’s central $3.84' \times 3.84'$ at $\lambda = 2.08$ m and $0.4''$ resolution covers a third of the total jet system and reveals two radio-luminous AGN, detected at $\sim 40\sigma$ significance.** We show the overarching jet axis (translucent white), determined from the northern lobe and southern hotspot (not shown), to scale for a jet radius of 1 kpc. The jet axis appears to pass through J152932.16+601534.4.

283 data reduction and results. We performed calibration with Source Peeling and Atmospheric Modeling [SPAM;
 284 13], starting out with the GSB data. After direction-dependent calibration, we used Python Blob Detection and
 285 Source Finder [PyBDSF; 14] to derive a sky model from the final GSB image, which subsequently served to initial-
 286 isalise the direction-dependent calibration of the GWB data. As SPAM was designed with narrow-band data
 287 in mind, following standard practice, we first split the GWB data along the frequency axis, yielding four sub-
 288 bands of 50 MHz width each. We then calibrated each subband independently. A joint image of four calibrated
 289 subbands revealed residual ionospheric artefacts from ILTJ153004.28+602423.2, the same bright source in the
 290 vicinity of the northern lobe mentioned earlier. To mitigate these artefacts, we subtracted (on a subband basis)
 291 all sources outside of a spherical cap with a $9'$ radius centred around J2000 right ascension $\varphi = 15h29m32.0s$ and
 292 declination $\theta = 60d15m33.0s$. We then jointly reimaged the four source-subtracted subbands with WSClean,
 293 using Briggs weighting 0. This resulted in the $4.3''$ -resolution image of Fig. 1’s bottom panel. The noise level is
 294 $\sigma = 3$ Jy deg $^{-2}$ at its lowest.

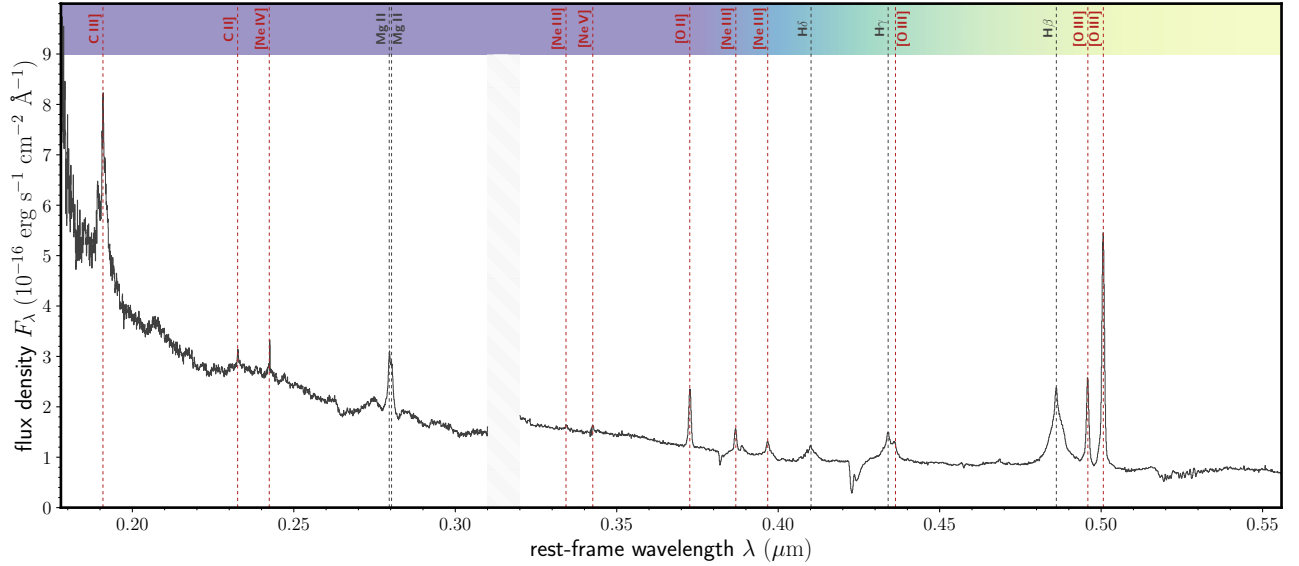
295 In the Legacy Survey DR10 optical imagery shown in Fig. 1’s bottom panel inset, we identified two faint
 296 galaxies in the arcsecond-scale vicinity of the southern host galaxy candidate. Of these, the galaxy at $(\varphi, \theta) =$
 297 $(232.37969^\circ, 60.26029^\circ)$ emits low-frequency radio emission at 6σ significance. At the $4.3''$ resolution of our
 298 fiducial uGMRT image, this radio emission is only narrowly separable from the host galaxy candidate’s, thus
 299 interfering with establishing the radio morphology of the candidate. Trading depth for resolution, we reim-

aged the uGMRT data with WSClean using Briggs weighting -0.5 , yielding a $3.6''$ resolution. Subsequently, to isolate the radio morphology of J152932.16+601534.4, we fit a circular Gaussian fixed at the sky coordinates of its radio-emitting neighbour. Naturally, we set this Gaussian’s full width at half maximum to $3.6''$. Upon subtracting the Gaussian, we obtained our final image; Fig. 2 shows its central region, where the noise level is $\sigma = 6 \text{ Jy deg}^{-2}$ at its lowest. Only the southern (and most radio-luminous) host galaxy candidate features an extension along the overarching jet axis seen in Fig. 1. (Radio luminosity L_ν is, at fixed redshift and large-scale halo mass, approximately proportional to jet power Q [2]. Under the Blandford–Znajek mechanism [15], $Q \propto M_\bullet^2$ (at fixed magnetic field strength and spin), where M_\bullet is the SMBH mass. As the generation of Porphyrior’s jets entails a significant SMBH mass gain $\Delta M_\bullet \sim 10^8\text{--}10^9 M_\odot$, the SMBH must now be massive; hence, a high radio luminosity is expected.) In our data, this extension — indicative of a pair of relativistically beamed jets — occurs at 5σ significance.

We estimated the probability to find a spurious (i.e. unrelated) radio-luminous AGN (RLAGN) with jets along Porphyrior’s overarching axis in the region where the host galaxy could plausibly reside. To find the sky density of RLAGN with discernible jet orientations at arcsecond-scale resolutions, metre-scale wavelengths, and 10^1 Jy deg^{-2} –scale noise levels, we studied the LoTSS DR1–derived RLAGN sample presented in Hardcastle *et al.* [16]. This sample, consisting of 23,344 RLAGN, contains 6,850 RLAGN with discernible jet orientations. The latter population’s *average* sky density $\bar{n}_s = 4 \cdot 10^{-3} \text{ arcmin}^{-2}$. Approximating the sky density n_s of spurious RLAGN with discernible jet orientations near Porphyrior’s host with \bar{n}_s would be appropriate only if such RLAGN would not cluster in the sky. More optimally, we estimated n_s by first counting, for each such RLAGN (that appears sufficiently far from the edges of the survey footprint), the number of neighbours in disks of radius $1'$. Next, we divided each count by the solid angle of the disks, and finally determined the sample mean: $n_s = 8 \cdot 10^{-3} \text{ arcmin}^{-2}$. (For disks of larger radii, n_s approaches \bar{n}_s .) We estimated the solid angle of the ‘strip’ in which an unrelated source could be mistaken for Porphyrior’s host to be $\Omega_s = 10^0 \times 10^{-1} \text{ arcmin}^2$. (We limited the strip’s angular length by asserting that plausible host candidates lie between Porphyrior’s two detected patches of jet emission.) Defining jets ‘aligned’ with Porphyrior’s when their position angle falls within a range of width 10^1 deg centred around Porphyrior’s position angle, the probability of randomly attaining alignment $p_s = \frac{10^\circ}{180^\circ} = 6 \cdot 10^{-2}$. One thus expects to encounter $\mathbb{E}[N_s] = n_s \cdot \Omega_s \cdot p_s = 4 \cdot 10^{-5}$ unrelated RLAGN with resolved and aligned jets near Porphyrior’s host. Assuming that N_s is Poisson-distributed, one or more such spurious sources appear with a probability $\mathbb{P}(N_s \geq 1) = 1 - e^{-\mathbb{E}[N_s]} \approx \mathbb{E}[N_s]$. (This approximation improves as $\mathbb{E}[N_s]$ decreases.) We thus find $\mathbb{P}(N_s \geq 1) = 4 \cdot 10^{-5}$; the probability to find a spurious *unresolved* RLAGN in the same region is $4 \cdot 10^1$ times larger. We conclude that J152932.16+601534.4 is Porphyrior’s host galaxy.

Keck I observations and data reduction The literature offers only photometric redshift estimates of the host galaxy. The SDSS DR12 [17] reports $z_p = 0.68 \pm 0.06$, the Legacy Surveys DR9 [18] reports $z_p = 0.93 \pm 0.08$, and Duncan [19] reports $z_p = 0.92 \pm 0.08$. For radio-emitting galaxies like J152932.16+601534.4, we consider the latter estimate to be most reliable.

To establish the redshift of Porphyrior’s host galaxy with certainty, we measured its (rest-frame) ultraviolet–optical spectrum with the Low Resolution Imaging Spectrometer [LRIS; 20–23] on the W. M. Keck Observatory’s Keck I Telescope. Adequate slit placement requires accurate knowledge of the galaxy’s coordinates. From the Legacy Surveys DR10 best-fit model, we found that J152932.16+601534.4’s centre lies at $(\varphi, \theta) = (232.38410^\circ, 60.25960^\circ)$. The galaxy’s half-light radius is $10.1 \pm 0.3 \text{ kpc}$. On 23 June 2023, we observed the galaxy for a total of 900 seconds. We used the 600/4000 grism on LRIS’ blue side, with 1×2 binning (spatial and spectral, respectively), and the 400/8500 grating on the red side, again with 1×2 binning. During the observations, the seeing was approximately $0.8''$; as we used a $1.5''$ slit, minimal slit losses occurred. Using a slit

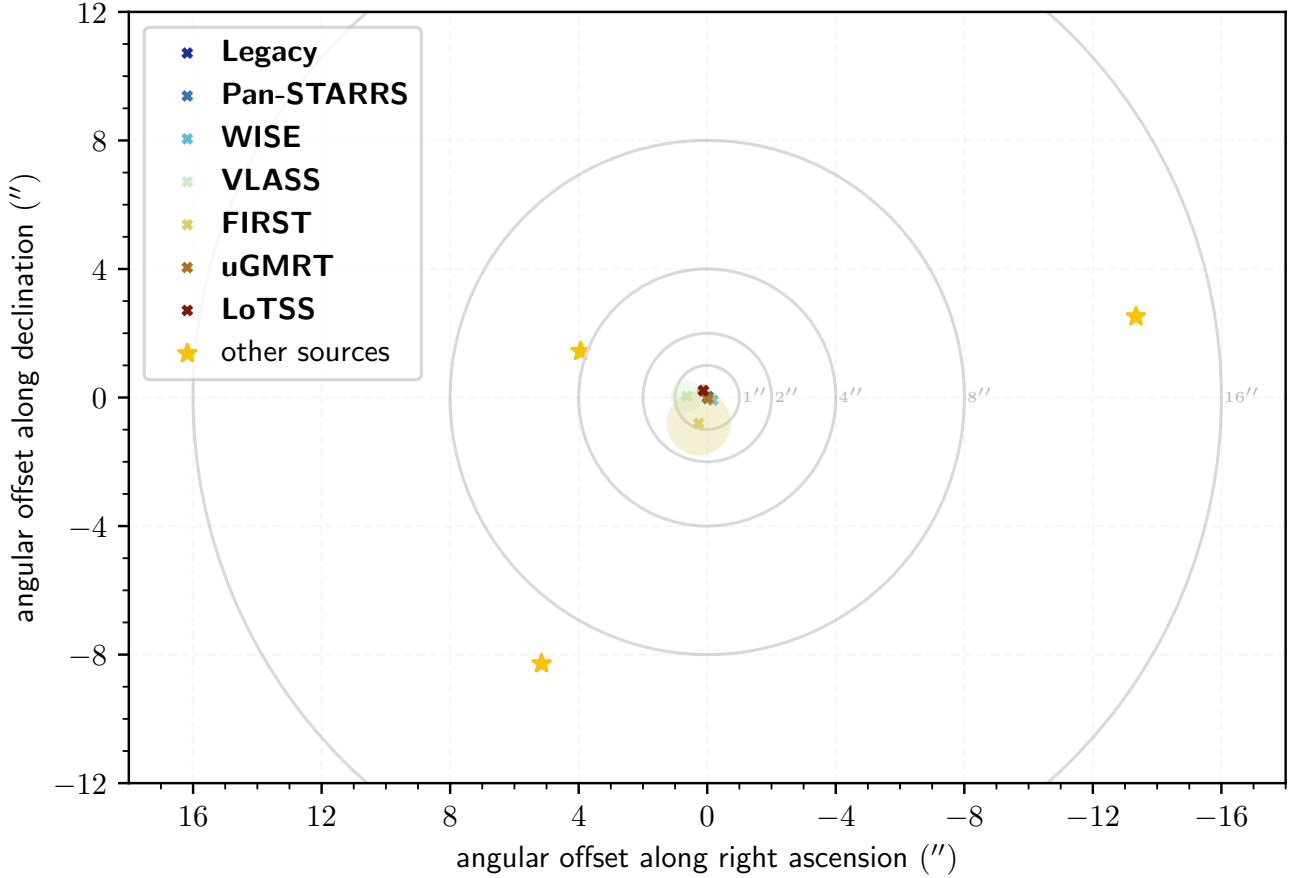


Extended Data Figure 3: **Ultraviolet–optical rest-frame spectrum of J152933.03+601552.5, the quasar-hosting galaxy 19'' north-northeast of J152932.16+601534.4, Porphyrior’s host galaxy.** We identify redshifted hydrogen, carbon, oxygen, neon, and magnesium lines, jointly implying $z_s = 0.799 \pm 0.001$. Forbidden lines from the quasar’s narrow-line region are shown in red. The spectrum has been measured with the LRIS on the W. M. Keck Observatory’s Keck I Telescope.

344 position angle of -70° , we could simultaneously obtain a spectrum for J152933.03+601552.5, the quasar-hosting
 345 galaxy which we initially considered (and then discarded) as a host candidate. We reduced the data with PypeIt
 346 [24], a Python-based pipeline with features tailored to reducing LRIS long-slit spectroscopy. We flat-fielded and
 347 sky-subtracted the data using standard techniques. We used internal arc lamps for wavelength calibration and a
 348 standard star for overall flux calibration.

349 The final LRIS-derived spectra of J152932.16+601534.4 and J152933.03+601552.5 are shown in Fig. 3 and Ex-
 350 tended Data Fig. 3, respectively. The corresponding spectroscopic redshifts are $z_s = 0.896 \pm 0.001$ and $z_s =$
 351 0.799 ± 0.001 . The uncertainties reflect LRIS’ limited spectral resolution as well as systematic errors in wave-
 352 length calibration. The latter spectroscopic redshift can be compared to the value derived for J152933.03+601552.5
 353 by the SDSS BOSS [25] on 5 July 2013. Visual inspection of the SDSS BOSS spectrum and its best fit indicates a
 354 robust spectroscopic redshift $z_s = 0.79836 \pm 5 \cdot 10^{-5}$. The two measurements are in agreement.

355 **Spectral energy distribution** To further assess the accretion mode of Porphyrior’s AGN, and to estimate
 356 its host’s stellar mass and possibly star formation rate (SFR), we performed spectral energy distribution (SED)
 357 inference. Through Vizier, the Astro Data Lab, and the NASA/IPAC Extragalactic Database, we collected cata-
 358 logued total (rather than fixed-aperture) flux densities, relative flux densities, magnitudes, Galactic transmission
 359 fractions, and total extinctions from rest-frame ultraviolet to radio wavelengths. Extended Data Fig. 4 shows the
 360 crossmatching results. It demonstrates that Porphyrior’s host galaxy (as identified in Legacy DR10) is, in view
 361 of the astrometric accuracies of the collected catalogue data, the only plausible match. Just $4.3''$ northeast from
 362 Porphyrior’s host galaxy lies another source, which could be either a Milky Way star or a galaxy. Mindful of the
 363 possibility of spuriously high flux density measurements as a result of target–neighbour blending, we assessed
 364 all images underlying the catalogued estimates by eye. The neighbouring source only appears to be a point of
 365 attention for flux density measurements at small wavelengths, such as in the Legacy g - and r -band, where it has



Extended Data Figure 4: **All flux densities used in the inference of Porphyrion’s host galaxy SED occur within an arcsecond of the Legacy DR10–identified host position.** Coloured disks show 1σ astrometric uncertainties, while grey circles denote angular distances from the Legacy DR10–identified host position. The golden stars mark all other Legacy DR10–identified sources in the angular vicinity of Porphyrion’s host.

366 flux densities $\sim 100\%$ and $\sim 60\%$ those of the target, respectively. At the Legacy z -band’s larger wavelengths,
 367 the neighbour’s flux density is small ($\sim 20\%$) relative to the target’s. The error induced by blending, which will
 368 add only a fraction of the neighbour’s flux density, should thus be negligible. Accordingly, the Pan-STARRS
 369 and WISE measurements at even larger wavelengths are not compromised by this neighbour.

370 We converted the Legacy relative flux densities to flux densities by multiplying with the reference flux density
 371 $F_\nu = 3631$ Jy. We converted the Pan-STARRS AB magnitudes to flux densities using the standard relation
 372 (e.g. Eq. 1 of Chambers *et al.* [26]). We converted the WISE relative flux densities to flux densities by multiplying
 373 with the reference flux densities of Jarrett *et al.* [27]’s Table 1. Extended Data Table 1 provides all retained flux
 374 densities F_ν and the central wavelengths λ they correspond to.

375 Porphyrion’s host galaxy lies at a Galactic latitude $b = 47.43194^\circ$. Fortunately, at these latitudes, the Galac-
 376 tic transmission is high for all bands included in our SED inference. We tabulate estimated transmitted fractions
 377 f_t in Extended Data Table 1. For Pan-STARRS i and y , we calculated f_t from total extinctions $A_\lambda = 0.022$ and
 378 $A_\lambda = 0.014$, respectively, via $f_t = 10^{-\frac{2}{5}A_\lambda}$. For Legacy g , where Galactic transmission is lowest, application of
 379 the correction factor f_t^{-1} results in a flux density increase of just $\sim 4\%$. For all bands, the correction is smaller
 380 than the flux density uncertainty. We conclude that, for our purposes, Galactic extinction can be neglected.

381 Next, using AGNfitter [31, Martínez-Ramírez *et al.* in prep.], we determined the SED posterior shown in

Extended Data Table 1: Flux densities F_ν of Porphyrior’s host galaxy throughout the electromagnetic spectrum. These are as measured, and thus have not been corrected for Galactic extinction; to do so, we provide Galactic transmission fractions f_t . Entries are sorted by the central wavelengths λ of the observing bands.¹

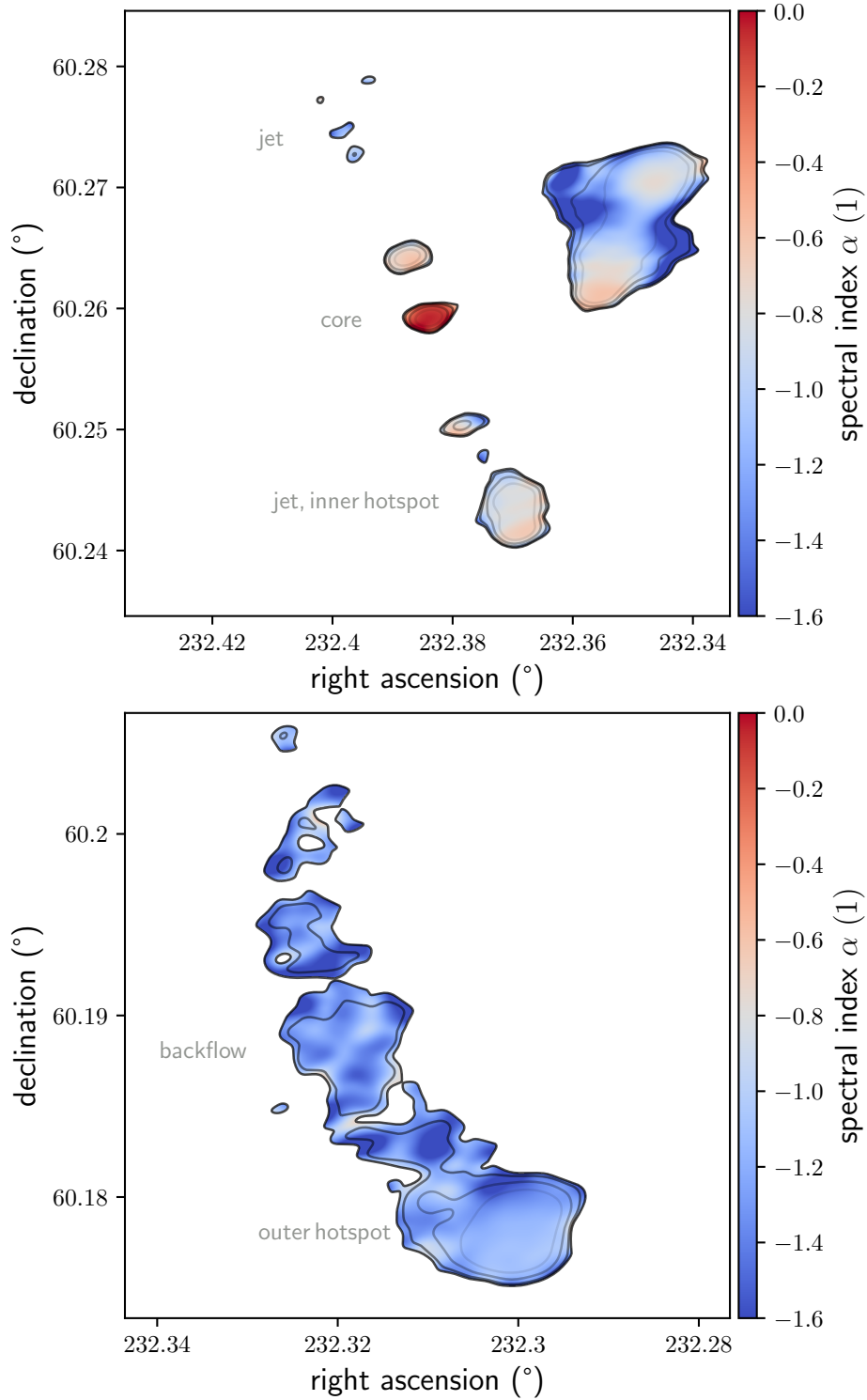
Band	λ (μm)	F_ν (Jy)	f_t (%)
Legacy g	$4.8 \cdot 10^{-1}$	$2.6 \pm 0.2 \cdot 10^{-6}$	96.3
Legacy r	$6.3 \cdot 10^{-1}$	$8.4 \pm 0.4 \cdot 10^{-6}$	97.5
Legacy z	$9.1 \cdot 10^{-1}$	$4.31 \pm 0.08 \cdot 10^{-5}$	98.6
Pan-STARRS i	$7.5 \cdot 10^{-1}$	$1.1 \pm 0.1 \cdot 10^{-5}$	98.0
Pan-STARRS y	$9.6 \cdot 10^{-1}$	$3.3 \pm 0.3 \cdot 10^{-5}$	98.7
WISE W ₁	$3.4 \cdot 10^0$	$2.41 \pm 0.02 \cdot 10^{-4}$	99.8
WISE W ₂	$4.6 \cdot 10^0$	$2.53 \pm 0.05 \cdot 10^{-4}$	99.9
WISE W ₃	$1.2 \cdot 10^1$	$8.1 \pm 0.5 \cdot 10^{-4}$	100
WISE W ₄	$2.2 \cdot 10^1$	$3.6 \pm 0.4 \cdot 10^{-3}$	100
VLASS	$1.0 \cdot 10^5$	$1.4 \pm 0.2 \cdot 10^{-3}$	100
FIRST	$2.1 \cdot 10^5$	$1.6 \pm 0.1 \cdot 10^{-3}$	100
uGMRT Band 4	$4.6 \cdot 10^5$	$2.1 \pm 0.1 \cdot 10^{-3}$	100
LoTSS	$2.1 \cdot 10^6$	$2.4 \pm 0.2 \cdot 10^{-3}$	100

When multiple flux densities or magnitudes from the same band were available in literature catalogues, we picked the highest signal-to-noise ratio measurement. Legacy data come from Dey *et al.* [18], Pan-STARRS data from Chambers *et al.* [26], WISE data from Lang *et al.* [28], VLASS data from Gordon *et al.* [29], FIRST data from Helfand *et al.* [30], uGMRT data from the present work, and LoTSS data from Shimwell *et al.* [4].

382 the bottom panel of Fig. 3. The posterior indicates the presence of a luminous SMBH accretion disk with an
383 obscuring torus, confirming the radiatively efficient nature of Porphyrior’s AGN. The SED posterior further
384 implies that the stellar mass of Porphyrior’s host is $M_\star = 6.7 \pm 1.4 \cdot 10^{11} M_\odot$. To gauge the sensitivity of
385 stellar mass estimates for this galaxy to methodological variation, we compare our result to the corresponding
386 stellar mass estimate in the LoTSS DR2 value-added catalogue [32]. This catalogue’s authors derive a stellar
387 mass $M_\star = 5.5_{-0.6}^{+0.7} \cdot 10^{11} M_\odot$ from SED fits to Legacy g , r , z and WISE W₁ and W₂ flux densities. (This
388 stellar mass estimate is not based on the spectroscopic redshift we have obtained through LRIS, but utilises
389 a photometry-based redshift posterior with mean and standard deviation $z_p = 0.92 \pm 0.08$ [19].) The two
390 stellar mass measurements are in agreement. Due to the lack of rest-frame far-infrared photometry, the SFR of
391 Porphyrior’s host is virtually unconstrained by the SED posterior.

392 **Radio luminosities and spectral indices** To determine metre-wavelength radio luminosities and a metre-
393 wavelength spectral index for Porphyrior, we first measured its flux densities in the 6.2'' ILT and 4.3'' uGMRT
394 images. We assumed flux scale uncertainties of 10% and 5%, respectively.

395 Summing over all structural components, the outflow’s total flux density at $\lambda = 2.08$ m is $F_\nu = 63 \pm 6$ mJy.
396 Its total radio luminosity at rest-frame wavelength $\lambda_r = 1.10$ m therefore is $L_\nu = 1.4 \pm 0.1 \cdot 10^{26}$ W Hz⁻¹;
397 the core radio luminosity, $L_\nu = 5.3 \pm 0.5 \cdot 10^{24}$ W Hz⁻¹, comprises $\sim 4\%$ of the total. The outflow’s total
398 flux density at $\lambda = 0.46$ m is $F_\nu = 12.0 \pm 0.6$ mJy. Its total radio luminosity at $\lambda_r = 0.24$ m therefore is
399 $L_\nu = 2.7 \pm 0.1 \cdot 10^{25}$ W Hz⁻¹; the core radio luminosity, $L_\nu = 4.7 \pm 0.2 \cdot 10^{24}$ W Hz⁻¹, comprises $\sim 17\%$
400 of the total. These data imply a metre-wavelength total spectral index $\alpha = -1.09 \pm 0.08$ and a core spectral
401 index $\alpha = -0.09_{-0.07}^{+0.08}$. Through spectral index-based interpolation, we estimated the total radio luminosity
402 at $\lambda_r = 2$ m to be $L_\nu = 2.8 \pm 0.3 \cdot 10^{26}$ W Hz⁻¹. This latter total radio luminosity is an important input for



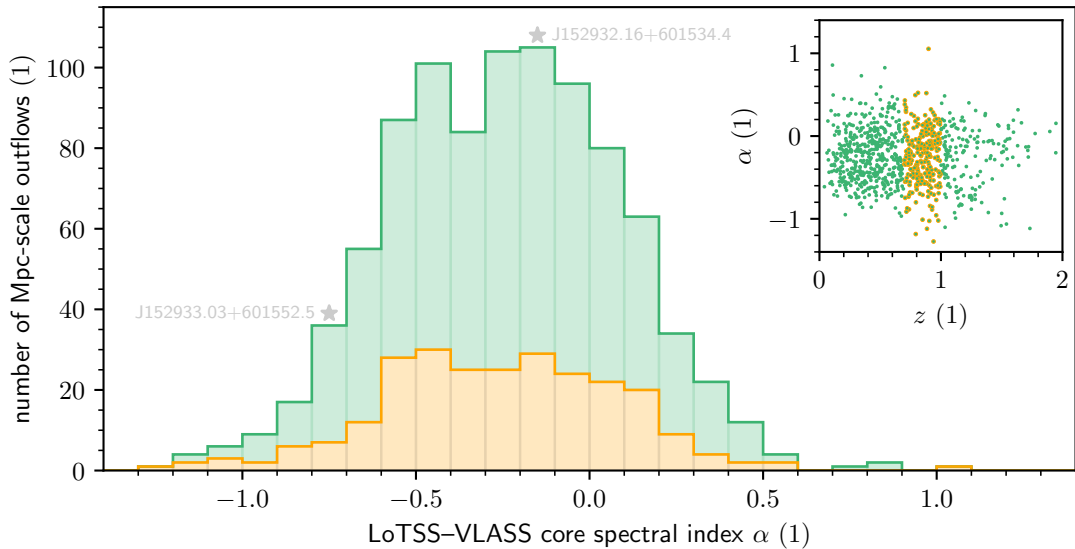
Extended Data Figure 5: **Metre-wavelength spectral indices around Porphyrior's centre and southern tip.** The top panel, which covers $3' \times 3'$, reveals synchrotron self-absorption at metre wavelengths in the host galaxy, consistent with the fuelling of powerful jets. The bottom panel, which covers $2' \times 2'$, reveals a hotspot with backflow. We show the mean spectral index α between 0.46–2.08 m, at a resolution of $6.2''$. From light to dark, the contours denote thermal noise-induced spectral index uncertainties of 0.05, 0.1, 0.2, and 0.3.

our dynamical modelling.

We calculated directionally resolved metre-wavelength spectral indices by combining the ILT and uGMRT images. Before doing so, we convolved the latter image to the former’s resolution. In Extended Data Fig. 5, we show two regions of interest from the resulting spectral index map, which consequently has a resolution of $6.2''$. To highlight the directions in which our spectral index measurements are informative, we blanked all directions in which the thermal noise–induced spectral index uncertainty exceeds 0.3. The top panel of Extended Data Fig. 5 shows that J152932.16+601534.4, Porphyrior’s host galaxy, has a significantly higher spectral index than J152933.03+601552.5, the aforementioned quasar-hosting galaxy. The former spectral index is consistent with zero, indicating that the onset of synchrotron self-absorption (SSA) in Porphyrior’s host galaxy occurs at metre wavelengths. By contrast, the onset of SSA in the quasar-hosting galaxy must occur at longer wavelengths, suggesting a lower lepton energy density and weaker magnetic fields in its synchrotron-radiating region. The bottom panel of Extended Data Fig. 5 shows that Porphyrior’s southern tip features much lower spectral indices, with a gradient along the jet axis. This gradient is consistent with a scenario of a hotspot with backflow in which spectral ageing occurs. Whereas $\alpha = -1.0 \pm 0.2$ at the hotspot’s southwestern side, the radio spectra gradually steepen to $\alpha = -1.6 \pm 0.2$ at the hotspot’s northeastern side. No spectral trend appears present further downstream.

We investigated more thoroughly whether the metre-wavelength spectral index discrepancy between J152932.16+601534.4 and J152933.03+601552.5 constitutes evidence that the former galaxy is Porphyrior’s host. For each of the $1.1 \cdot 10^4$ Mpc-scale outflows catalogued by Mostert *et al.* [33], we sought to determine LoTSS DR2 and VLASS core flux densities. LoTSS DR2 core flux densities were available for 1, 238 Mpc-scale outflows, whilst VLASS core flux densities were available for 6, 882. We found 924 Mpc-scale outflows for which both core flux densities were available; for these, we computed 144 MHz–3 GHz spectral indices. Extended Data Fig. 6 summarises the results. The sample mean and standard deviation are -0.25 and 0.33 , respectively; the median is -0.24 , and 68% of all spectral indices lie between -0.58 and 0.09 . It is likely that some VLASS-detected cores are undetectable in the LoTSS DR2 because of a combination of low VLASS flux densities and flat ($\alpha \simeq 0$) or ‘inverted’ ($\alpha > 0$) radio spectra. The consequence is a bias in Extended Data Fig. 6 towards lower spectral indices. By requiring that the LoTSS DR2 core is an isolated source on the sky, the core spectral indices of Fanaroff–Riley (FR) I outflows have likely been selected out. As Porphyrior is an FR II outflow, deselecting FR I outflows may have the beneficial effect of making the distribution more representative of the object under study here. As shown in Extended Data Fig. 6’s inset, the spectral indices in this sample do not exhibit a strong trend with redshift. Consequently, no major distributional changes occurred when we restricted the sample to the 254 Mpc-scale outflows whose redshifts differ at most $\Delta z = 0.1$ from those of either J152932.16+601534.4 or J152933.03+601552.5 (Extended Data Fig. 6’s orange histogram). We conclude that the known core spectral indices of Mpc-scale outflows favour J152932.16+601534.4 over J152933.03+601552.5 as Porphyrior’s host, strengthening our earlier identification.

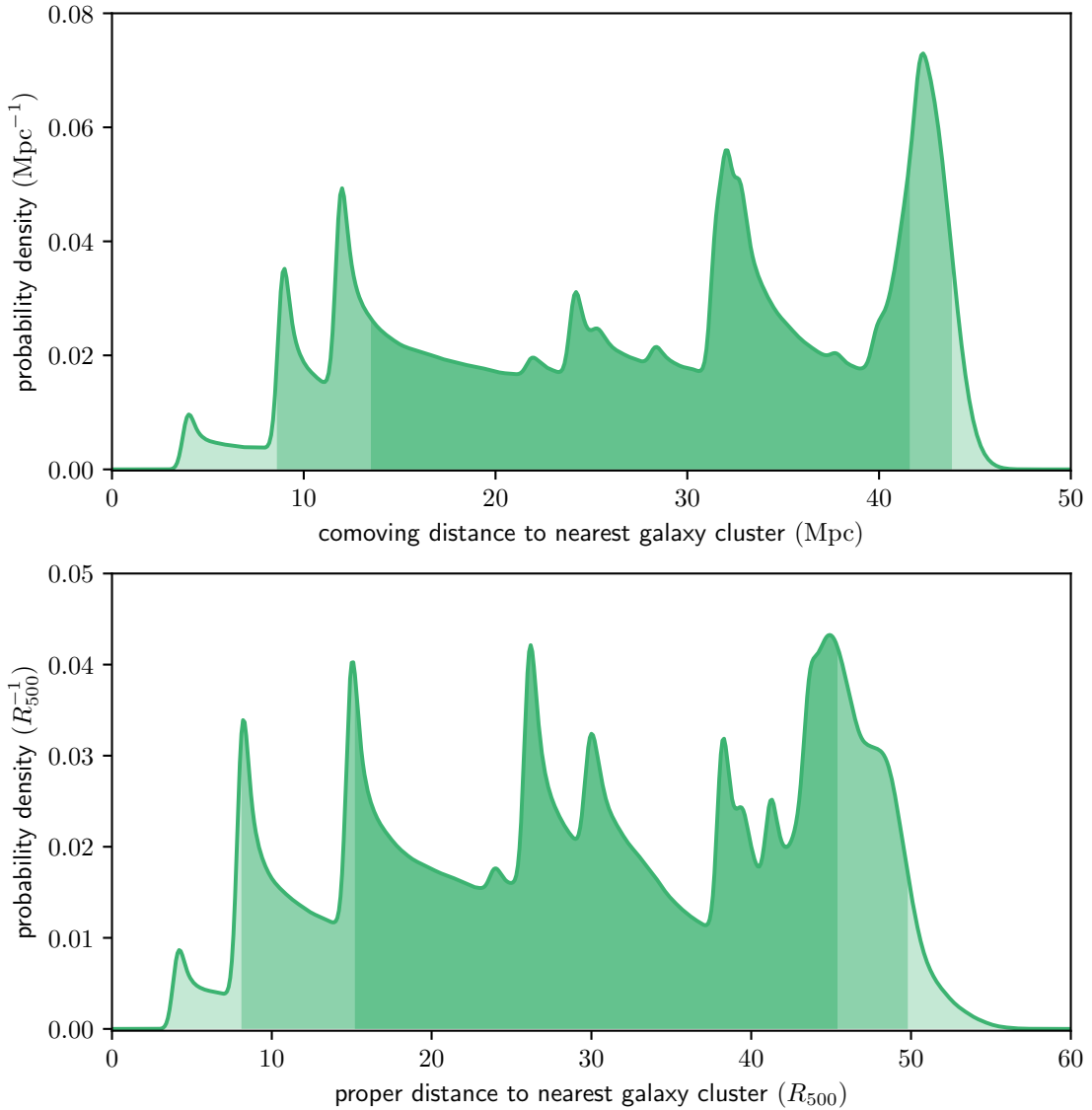
Cosmic Web environment Cosmic Web environment characterisations of luminous ($L_\nu(\nu = 150 \text{ MHz}) \geq 10^{24} \text{ W Hz}^{-1}$) Mpc-scale outflows in the Local Universe ($z \lesssim 0.2$) have recently been obtained [34] by localisation in Bayesian large-scale structure reconstructions and by crossmatching with catalogues of galaxy clusters ($M_{500} \geq 0.6 \cdot 10^{14} M_\odot$) and galaxy groups ($M_{500} < 0.6 \cdot 10^{14} M_\odot$). The resulting probability distribution over Cosmic Web environments serves as a prior distribution for Porphyrior’s Cosmic Web environment. In the Local Universe, $\sim 30\%$ of all luminous Mpc-scale outflows reside in clusters, $\sim 60\%$ in groups, and the remaining $\sim 10\%$ in more dilute parts of filaments, in sheets, or in voids [34]. Thus, if this probability distribution does not evolve with redshift and a cluster environment can be excluded, Porphyrior likely originates from a filament. To evaluate whether Porphyrior’s host galaxy inhabits a cluster, we extracted right ascensions,



Extended Data Figure 6: **LoTSS–VLASS spectral index distribution of the cores of 924 Mpc-scale outflows.** In grey, we indicate the bins in which the core spectral indices of J152932.16+601534.4, Porphyrior’s claimed host galaxy, and J152933.03+601552.5 fall. The distribution suggests that the core spectral index of J152932.16+601534.4 ($\alpha = -0.18 \pm 0.06$) is more typical of Mpc-scale outflows than the core spectral index of J152933.03+601552.5. (For J152933.03+601552.5, due to a VLASS non-detection, we show the LoTSS–uGMRT Band 4 spectral index.) The inset shows the same data as a function of redshift z . The orange subsample comprises Mpc-scale outflows whose redshifts differ at most $\Delta z = 0.1$ from those of either J152932.16+601534.4 or J152933.03+601552.5.

447 declinations, redshifts, and R_{500} -radii from the cluster catalogue of Wen & Han [35], which is based on Legacy
 448 DR10. Even though these data allow for cluster detections up to $z \sim 1.5$, we did not find a cluster close to
 449 Porphyrior’s host. To reach this conclusion statistically, we first estimated cluster redshift uncertainties using
 450 $\sigma_z(z) = 0.02 \cdot \frac{z}{0.9} \cdot (1 + z)$ for photometric cluster redshifts, as suggested by the bottom-right panel of Fig. 7
 451 of Wen & Han [35], and $\sigma_z = 0.001$ for spectroscopic cluster redshifts. We neglected uncertainties in cluster
 452 right ascensions and declinations. We then Monte Carlo–simulated a redshift for both Porphyrior’s host and
 453 all clusters (assuming Gaussian redshift distributions), converted right ascensions, declinations, and redshifts
 454 into comoving coordinates, and finally identified the cluster nearest to Porphyrior’s host. We recorded the co-
 455 moving distance to this cluster as well as the ratio between the corresponding proper distance and the cluster’s
 456 R_{500} -radius. We repeated this Monte Carlo procedure millions of times, until the probability distributions over
 457 these distance measures converged. The results are shown in Extended Data Fig. 7. Around Porphyrior’s red-
 458 shift, the Wen & Han [35] photometric cluster redshift uncertainties $\sigma_z \approx 0.04$, large enough to force us to
 459 consider several clusters as candidates for being the nearest. Each peak corresponds to the smallest possible dis-
 460 tance to a possibly nearest cluster. The peak location is determined by both the angle between Porphyrior’s
 461 host and the cluster and by Porphyrior’s redshift. In Monte Carlo realisations such that the cluster redshift
 462 matches Porphyrior’s, the distance is minimal. The nearest cluster lies at a comoving distance of 30^{+12}_{-17} Mpc, or
 463 31^{+14}_{-16} cluster radii (68% probability intervals); the nearest cluster lies at a comoving distance of 30^{+14}_{-22} Mpc, or
 464 31^{+19}_{-23} cluster radii (95% probability intervals). In just 0.1% of all realisations, Porphyrior’s host is five or fewer
 465 R_{500} -radii away from the nearest cluster.

466 To investigate whether a filament or a void environment is more probable, we performed probabilistic galaxy
 467 counts using the Legacy data underlying the Wen & Han [35] cluster catalogue. We extracted right ascensions,



Extended Data Figure 7: **DESI Legacy Imaging Surveys DR10 galaxy cluster redshift uncertainties induce multi-modal, asymmetric probability distributions over measures of distance between Porphyrior’s host galaxy and the nearest galaxy cluster.** We mark median-centred intervals containing 68% and 95% of all probability. The data suggest that Porphyrior does not originate from a cluster.

468 declinations, redshift posterior means, and redshift posterior standard deviations of all Legacy-detected galaxies
 469 that lie within 1.5° of Porphyrior’s host. In a similar spirit as before, we then Monte Carlo–simulated redshifts
 470 (where, for simplicity, we approximated the galaxies’ redshift posterior distributions with Gaussian distribu-
 471 tions), converted right ascensions, declinations, and redshifts into comoving coordinates, and counted the num-
 472 ber of Legacy-detected galaxies (excluding Porphyrior’s host) within a sphere of given radius centred around
 473 Porphyrior’s host. To properly take into account galactic redshift uncertainties, we repeated this Monte Carlo
 474 procedure 1,000 times. In a sphere with a comoving radius of 10 Mpc centred around Porphyrior’s host, we
 475 counted 35 ± 6 other Legacy-detected galaxies. We then performed analogous probabilistic galactic neighbour
 476 counts for a control sample of galaxies at comparable redshifts. We selected controls by demanding that their red-

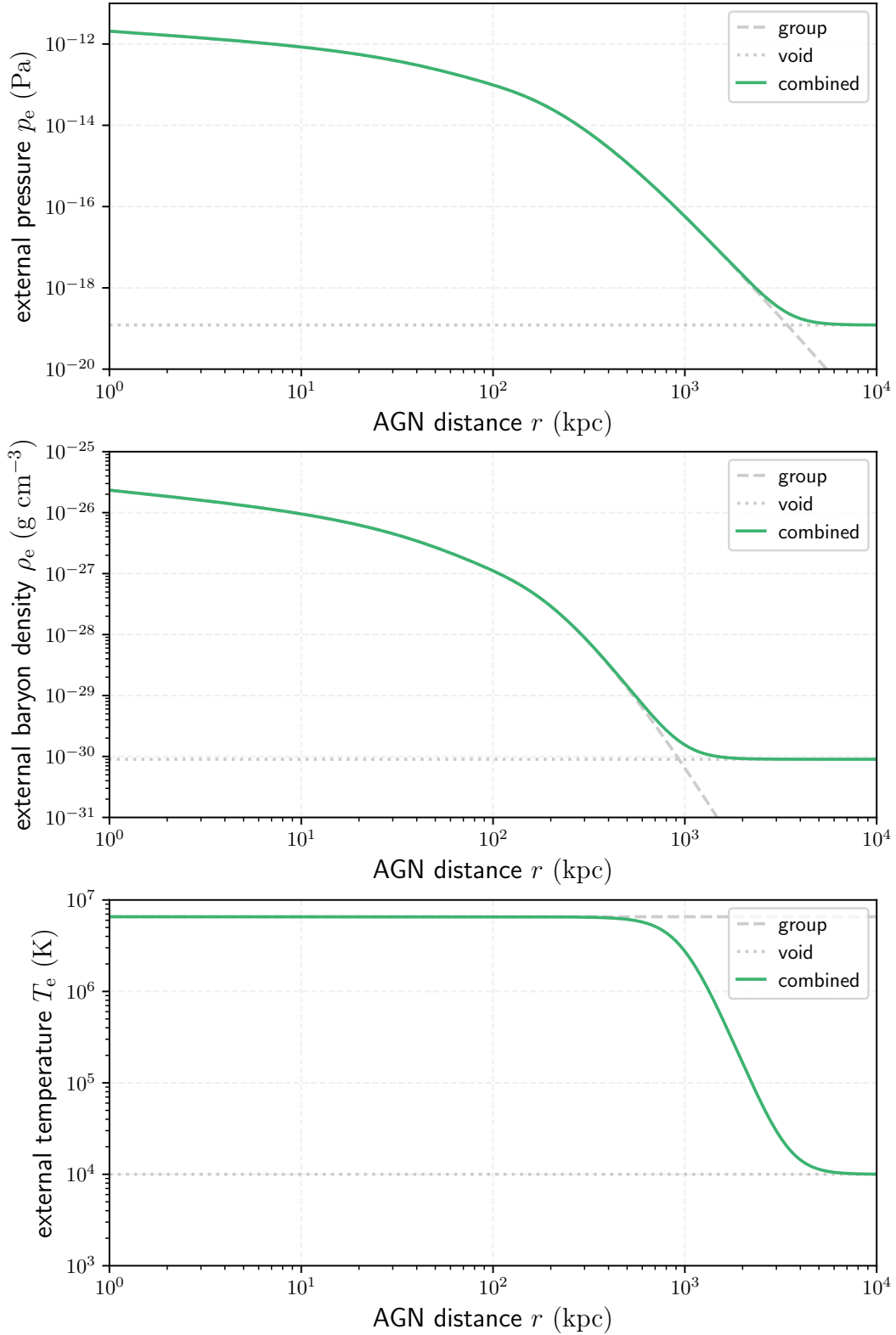
477 shift means do not deviate more than 0.05 from Porphyrior’s. To ensure that these mean redshifts are reliable,
 478 we further demanded that the redshift standard deviations of controls are less than 0.1. From the available candi-
 479 dicate controls, we picked 100 controls at random, and performed the counts for them. Porphyrior’s galactic
 480 neighbour count, relative to those of the control sample, occurs at percentile $42_{-23}^{+26}\%$. If we assume that cir-
 481 cumgalactic Cosmic Web density is a monotonic function of the number of galactic neighbours, Porphyrior’s
 482 circumgalactic Cosmic Web density percentile will be $42_{-23}^{+26}\%$, too. This suggests that Porphyrior does not
 483 originate from a void. In line with the expectation for luminous Mpc-scale outflows in the Local Universe, we
 484 conclude that Porphyrior most likely originates from a filament.

485 **Dynamical modelling: jet power and age** We derived Porphyrior’s jet power and age from its length, ra-
 486 dio luminosity, cosmological redshift, and likely environment by fitting evolutionary tracks. We generated these
 487 evolutionary tracks with the simulation-based analytic outflow model of Hardcastle [2]. This model requires as-
 488 sumptions on the large-scale environment in which the dynamics take place. Following the previous section, we
 489 suppose that the host galaxy resides in the centre of a galaxy group of mass $M_{500} = 10^{13} M_{\odot}$ (which comprises
 490 contributions from both dark and baryonic matter) [34, 36]. We assigned the group a universal pressure profile
 491 [UPP; 37] $p_g(r)$, which can be parametrised just by M_{500} . (Sun *et al.* [38] have shown that the UPP applies to
 492 galaxy groups, even though the profile has originally been proposed to fit data on galaxy clusters — which have
 493 much higher masses: $10^{14} M_{\odot} < M_{500} < 10^{15} M_{\odot}$.) To obtain the group’s baryon density profile from its
 494 pressure profile, we invoked the ideal gas law: $\rho_g(r) = \frac{p_g(r)\langle m \rangle}{k_B T_g}$, where $\langle m \rangle$ is the average plasma particle mass
 495 and T_g the group temperature. We assumed a pure ^1H – ^4He plasma with a ^4He mass fraction $Y = 25\%$ [e.g.
 496 39], so that $\langle m \rangle \approx \frac{4}{8-5Y} m_p = 0.6 m_p$, where m_p is the proton mass. We estimated T_g , which we assumed
 497 constant in space and time, using the mass–temperature relation specified by Eq. 9 and Tables 3 and 4 of Lovisari
 498 *et al.* [40]:

$$\frac{k_B T_g}{2 \text{ keV}} = 0.77 \cdot \left(\frac{M_{500}}{5 \cdot 10^{13} h_{70}^{-1} M_{\odot}} \right)^{0.61}. \quad (1)$$

499 The aforementioned mass implies $T_g = 7 \cdot 10^6$ K. As Mpc-scale outflows reach beyond the edges of groups,
 500 it was also necessary to estimate the pressure and baryon density in the AGN’s more distant surroundings. Fol-
 501 lowing the bottom-right panel of Ricciardelli *et al.* [41]’s Fig. 6, we set the baryon overdensity within voids at
 502 Porphyrior’s redshift to $\delta = -0.7$. (In doing so, we implicitly assumed that the baryonic matter overdensity
 503 field is identical to the total matter overdensity field — which comprises contributions from both dark and
 504 baryonic matter — as Ricciardelli *et al.* [41] considers the latter.) We obtained a void baryon density $\rho_v =$
 505 $\rho_{c,0} \Omega_{\text{BM},0} (1+z)^3 (1+\delta) = 9 \cdot 10^{-31} \text{ g cm}^{-3}$, where $\rho_{c,0}$ is today’s critical density. Following Upton Sander-
 506 beck *et al.* [42]’s detailed study of IGM temperatures through cosmic time, which suggests a void temperature
 507 $T_v \sim 10^3$ – 10^4 K at Porphyrior’s redshift, we set $T_v = 1 \cdot 10^4$ K. This choice reflects the fact that we are inter-
 508 ested in void temperatures near the galaxy group. Again applying the ideal gas law, and taking $\langle m \rangle$ as before, we
 509 obtained a void pressure $p_v = 1 \cdot 10^{-19}$ Pa. Finally, we defined the external pressure $p_e(r) = p_g(r) + p_v$, baryon
 510 density $\rho_e(r) = \rho_g(r) + \rho_v$, and baryon density–weighted temperature $T_e(r) = \frac{\rho_g(r)T_g + \rho_v T_v}{\rho_e(r)}$. Extended Data
 511 Fig. 8 shows these profiles.

512 We explored whether the addition of a filament component would significantly change Extended Data
 513 Fig. 8’s profiles. We assumed a baryon overdensity $\delta = 10$ at the filament spine, and baryon density and temper-
 514 ature profiles following Tuominen *et al.* [43]’s results for massive filaments in the EAGLE simulation. We found
 515 pressure and baryon density contributions of an importance similar to or lesser than that of the group, even at
 516 Mpc-scale distances. We thus considered the addition of the filament unnecessary, especially in light of model



Extended Data Figure 8: **Pressure, baryon density, and temperature external to the outflow, as a function of the proper distance from Porphyrior's AGN, in our dynamical modelling.** The profiles consist of contributions from the outflow's presumed galaxy group and the adjacent voids.

517 uncertainties such as the group's mass and the surmised validity of extrapolating the group's UPP to Mpc-scale
518 distances.

519 We generated 21 evolutionary tracks of 200 time steps each, spanning a range jet powers $Q = 10^{38.8-}$
520 $10^{39.2}$ W. Propagating total length and radio luminosity uncertainties, we obtained $Q = 1.3 \pm 0.1 \cdot 10^{39}$ W
521 and $T = 1.9_{-0.2}^{+0.7}$ Gyr. The outflow's jet power uncertainty is set by radio luminosity uncertainty while its age
522 uncertainty is set by total length uncertainty. The inferred Gyr-scale age suggests that treating outflow evolution
523 as a process at a single redshift — as is currently done in the model of Hardcastle [2] — is crude for the largest
524 outflows, and may need revision. Each jet's average speed $\langle \beta \rangle := \frac{\langle v \rangle}{c} = \frac{l}{2cT} = 0.58_{-0.07}^{+0.04}\%$, where c is the speed
525 of light. The energy transported by the jets $E = QT = 7.6_{-0.7}^{+2.1} \cdot 10^{55}$ J. As a black hole can redirect at most
526 half of the rest energy of infalling matter to electromagnetic radiation and jet fuelling, and the energy an RE
527 AGN spends on electromagnetic radiation must at least equal the energy spent on jet fuelling, the black hole
528 must have gained a mass $\Delta M_{\bullet} > 2 \frac{E}{c^2} = 8.5_{-0.8}^{+2.4} \cdot 10^8 M_{\odot}$ while powering the jets.

529 **Total outflow length** To estimate Porphyron's total length from its projected length, we perform statistical
530 deprojection. Equation 9 of Oei *et al.* [44] stipulates the probability density function (PDF) of an outflow's total
531 length random variable (RV) L in case its projected length RV L_p is known to equal some value l_p . This PDF
532 is parametrised by the tail index ξ of the Pareto distribution assumed to describe L . We calculate the median
533 and expectation value of $L | L_p = l_p$ for tail indices $\xi = -3$ and $\xi = -4$, the integer values closest to the
534 observationally favoured $\xi = -3.5 \pm 0.5$ [44].

535 First, we determine the cumulative distribution function (CDF) of $L | L_p = l_p$ through integration:

$$536 \begin{aligned} F_{L|L_p=l_p}(l) &:= \int_{-\infty}^l f_{L|L_p=l_p}(l') dl' & (2) \\ &= \frac{-\xi}{2^{1+\xi}\pi} \frac{\Gamma^2\left(-\frac{\xi}{2}\right)}{\Gamma(-\xi)} \int_1^{\max\{x,1\}} \frac{x'^{\xi-1}}{\sqrt{x'^2-1}} dx', \end{aligned}$$

536 where $x := \frac{l}{l_p}$ and $x' := \frac{l'}{l_p}$.

537 For $\xi = -3$, the CDF concretises to

$$538 \begin{aligned} F_{L|L_p=l_p}(l) &= \frac{3}{2} \int_1^{\max\{x,1\}} \frac{dx'}{x'^4 \sqrt{x'^2-1}} & (3) \\ &= \begin{cases} 0 & \text{if } x < 1; \\ \frac{(2x^2+1)\sqrt{x^2-1}}{2x^3} & \text{if } x \geq 1. \end{cases} \end{aligned}$$

538 The median conditional total length, l_m , is defined by $F_{L|L_p=l_p}(l_m) := \frac{1}{2}$. Numerically, we obtain $x_m := \frac{l_m}{l_p} \approx$
539 1.0664 , or $l_m \approx 1.0664 l_p$. As $l_p = 6.43 \pm 0.05$ Mpc, we find $l_m = 6.86 \pm 0.05$ Mpc. An analogous numerical
540 determination of the 16-th and 84-th percentiles then yields $l = 6.9_{-0.4}^{+1.6}$ Mpc.

541 For $\xi = -4$, the CDF concretises to

$$542 \begin{aligned} F_{L|L_p=l_p}(l) &= \frac{16}{3\pi} \int_1^{\max\{x,1\}} \frac{dx'}{x'^5 \sqrt{x'^2-1}} & (4) \\ &= \begin{cases} 0 & \text{if } x < 1; \\ \frac{2}{3\pi} \left(\frac{(3x^2+2)\sqrt{x^2-1}}{x^4} + 3 \arccos \frac{1}{x} \right) & \text{if } x \geq 1. \end{cases} \end{aligned}$$

542 Numerically, we obtain $x_m \approx 1.0515$, or $l_m \approx 1.0515 l_p$, and thus $l_m = 6.76 \pm 0.05$ Mpc. In the same way
 543 as before, we find $l = 6.8_{-0.3}^{+1.2}$ Mpc.

544 Equation 10 of Oei *et al.* [44] gives a closed-form expression for $\mathbb{E}[L | L_p = l_p](\xi)$. Table 1 of the same
 545 work lists $\mathbb{E}[L | L_p = l_p](\xi = -3) = \frac{3\pi}{8} l_p$ and $\mathbb{E}[L | L_p = l_p](\xi = -4) = \frac{32}{9\pi} l_p$. In the case of Porphyryon,
 546 these expressions concretise to $\mathbb{E}[L | L_p = l_p](\xi = -3) = 7.58 \pm 0.06$ Mpc and $\mathbb{E}[L | L_p = l_p](\xi = -4) =$
 547 7.28 ± 0.05 Mpc.

548 By conditioning L on more knowledge than a value for L_p alone, statistical deprojection could be made
 549 more precise. For example, one could additionally condition on the fact that Porphyryon is generated by a Type
 550 2 radiatively efficient (RE) AGN. If Type 1 RE AGN are seen mostly face-on and Type 2 RE AGN are seen
 551 mostly edge-on, as proposed by the unification model [e.g. 45], then the detection of a Type 2 RE AGN would
 552 imply that the jets make a small angle with the sky plane. Extending the formulae to include this knowledge
 553 is beyond the scope of this work; however, mindful of the associated deprojection factor-reducing effect, we
 554 choose $\xi = -4$ as our fiducial tail index.

555 To assess Porphyryon's transport capabilities in a cosmological context, it is instructive to calculate its length
 556 relative to Cosmic Web length scales. In particular, the outflow's total length relative to the typical cosmic
 557 void radius at its epoch is $f_v := l(1+z)R_v^{-1}$, where R_v is the typical comoving cosmic void radius. For
 558 $l = 6.8_{-0.3}^{+1.2}$ Mpc, $z = 0.896 \pm 0.001$, and $R_v = 20$ Mpc [46], we find $f_v = 64_{-2}^{+12}$ %. For our fiducial total
 559 length $l = 7$ Mpc, we find $f_v = 66$ %.

560 **Filament shape modification** We predict that powerful, long-lived outflows like Porphyryon cause their host
 561 galaxies' filaments to expand thermally. Through lateral shocks, the jets distribute an amount of heat Q_{WHIM}
 562 over the warm-hot IGM. This medium is sufficiently dilute that plasma interactions can be neglected; as a
 563 result, the ideal gas law, $pV = Nk_B T$, may be adopted as the equation of state. Here, p , V , N , and T are the
 564 filament's pressure, volume, plasma particle number, and temperature, respectively; k_B is Boltzmann's constant.
 565 Assuming a thermodynamic process at constant pressure and particle number, the work W is

$$W = p\Delta V = Nk_B\Delta T. \quad (5)$$

566 Before the outflow's emergence, the filament's equation of state is $pV_i = Nk_B T_i$, where V_i and T_i are its initial
 567 volume and temperature, respectively. Upon dividing Eq. 5 by this equation of state, one obtains

$$\frac{\Delta V}{V_i} = \frac{\Delta T}{T_i}. \quad (6)$$

568 Assuming that the filament retains a cylindrical shape, initially with radius r_i and finally with radius r_f , and
 569 using that $\Delta V := V_f - V_i$, one obtains

$$\frac{r_f}{r_i} = \sqrt{1 + \frac{\Delta T}{T_i}}. \quad (7)$$

570 The radius ratio, $\frac{r_f}{r_i}$, depends only on the ratio between the temperature increase $\Delta T := T_f - T_i$ and the initial
 571 temperature. The temperature increase is

$$\Delta T = \frac{Q_{\text{WHIM}}}{NC_{p,m}}, \quad (8)$$

572 where $C_{p,m}$ is the molar heat capacity at constant pressure. For a monatomic gas or a hydrogen plasma, $C_{p,m} =$
573 $\frac{5}{2}R$, where R is the molar gas constant. The number of filamentary electrons and atomic nuclei affected by the
574 outflow is

$$N = \frac{\pi r_i^2 L \rho_i}{\mu m_p}, \quad (9)$$

575 where L is the length of the cylindrical segment affected, ρ_i is the initial baryonic mass density, μ is the average
576 mass of a plasma particle relative to the proton mass, and m_p is the proton mass. We estimate $\frac{L}{2}$ by multiplying
577 the typical speed of lateral shocks with the outflow's lifetime. We decompose $\rho_i = \rho_{c,0} \Omega_{\text{BM},0} (1+z)^3 (1+\delta)$,
578 where z and δ are the filament's cosmological redshift and baryonic overdensity, respectively.

579 To estimate Q_{WHIM} given E , the total energy carried by the jets up to the time of observation, we turn to
580 analytical models and numerical simulations. Modelling indicates that just $\sim 10\%$ of the total energy is lost
581 through radiative processes [2]. This fraction increases with redshift, as inverse-Compton losses to the CMB
582 become more pronounced. Numerical simulations show that, at least in galaxy clusters, $\sim 50\%$ of the non-
583 radiated energy is converted into thermal or kinetic energy carried by the shocked medium, and the other $\sim 50\%$
584 is converted into thermal or kinetic energy carried by the outflow's lobes [47]. Over time, the kinetic energy turns
585 into thermal energy. It is, at present, unclear how fast remnant lobes mix with the surrounding medium, and
586 how the mixing timescale varies with the latter's density. Here we assume that, at late times, all of the lobes'
587 energy mixes with the surrounding medium. As such, we estimate $Q_{\text{WHIM}} \rightarrow 90\% \cdot E$.

588 We assess the outflow-induced morphological change to Porphyryon's filament by evaluating Eq. 7, taking
589 $Q_{\text{WHIM}} = 7 \cdot 10^{55}$ J, $r_i \approx r_c = 1.2$ Mpc (a typical filament core radius [43]), $L = 2 \cdot 7$ Mpc = 14 Mpc
590 (assuming that the region beyond the outflow's direct reach that is affected at late times is comparable in length
591 to the outflow itself), $z = 0.9$, $1 + \delta = 10$, $\mu = 0.5$, and $T_i = 10^7$ K; we find $\Delta T = 3 \cdot 10^7$ K (an increase of
592 $\sim 300\%$) and $r_f = 2.4$ Mpc (an increase of $\sim 100\%$). Porphyryon's heat dissipation renders the outflow's native
593 filament much hotter and thicker than it would have otherwise been.

594 For our cosmological outlook, we assumed a typical jet power and age that are each an order of magni-
595 tude lower than Porphyryon's. We thus estimated the combined energy carried by 10 Mpc-scale outflows to be
596 $Q_{\text{WHIM}} = 7 \cdot 10^{54}$ J. Assuming non-overlapping affected regions, we estimated $L = 10 \cdot 2 \cdot 1$ Mpc = 20 Mpc.
597 Leaving all other parameters identical, we find $\Delta T = 2 \cdot 10^6$ K (an increase of $\sim 20\%$) and $r_f = 1.3$ Mpc (an
598 increase of $\sim 10\%$).

599 **Quasar mass–based host galaxy candidate elimination** SDSS J152933.03+601552.5 is the quasar-hosting
600 galaxy 19'' north-northeast of J152932.16+601534.4, the galaxy we have identified as Porphyryon's host. We ini-
601 tially also considered SDSS J152933.03+601552.5 as a host galaxy candidate. However, aforementioned arguments
602 involving the presence of jets and their orientation and, to a lesser degree, arguments involving core radio lumi-
603 nosity and core synchrotron self-absorption all favour J152932.16+601534.4. We now discuss how our results
604 would change if, instead, SDSS J152933.03+601552.5 were Porphyryon's host galaxy. Doing so will lead to a con-
605 tradiction that disproves this alternative hypothesis.

606 First, we discuss results that do not require dynamical modelling. To start with, Porphyryon would remain
607 generated by an RE AGN. The host galaxy redshift would decrease from $z = 0.896 \pm 0.001$ to $z = 0.799 \pm$
608 0.001 , decreasing Porphyryon's projected length from $l_p = 6.43 \pm 0.05$ Mpc to $l_p = 6.21 \pm 0.05$ Mpc. Again
609 using $\xi = -4$, the total length would decrease from $l = 6.8_{-0.3}^{+1.2}$ Mpc to $l = 6.5_{-0.3}^{+1.2}$ Mpc and its conditional
610 expectation from $\mathbb{E}[L | L_p = l_p] = 7.28 \pm 0.05$ Mpc to $\mathbb{E}[L | L_p = l_p] = 7.03 \pm 0.06$ Mpc. If orientation
611 distinguishes Type 1 from Type 2 RE AGN, as the unification model supposes, then these statistical deprojection

612 results may underestimate Porphyrior’s total length. Porphyrior would remain the projectively longest galaxy-
613 made structure identified so far. The host’s stellar mass would decrease from $M_{\star} = 6.7 \pm 1.4 \cdot 10^{11} M_{\odot}$ to
614 $M_{\star} = 4.0_{-0.3}^{+0.3} \cdot 10^{11} M_{\odot}$, while the SFR would become $S = 4.9_{-0.4}^{+0.3} \cdot 10^1 M_{\odot} \text{ yr}^{-1}$ [48]. Porphyrior’s total
615 radio luminosity at rest-frame wavelength $\lambda_r = 2 \text{ m}$ would decrease from $L_{\nu} = 2.8 \pm 0.3 \cdot 10^{26} \text{ W Hz}^{-1}$ to
616 $L_{\nu} = 2.2 \pm 0.2 \cdot 10^{26} \text{ W Hz}^{-1}$.

617 Next, we discuss results that come from dynamical modelling. The jet power would decrease from $Q =$
618 $1.3 \pm 0.1 \cdot 10^{39} \text{ W}$ to $Q = 1.0 \pm 0.1 \cdot 10^{39} \text{ W}$, while the age would slightly increase from $T = 1.9_{-0.2}^{+0.7} \text{ Gyr}$ to
619 $T = 1.9_{-0.1}^{+0.7} \text{ Gyr}$. The transported energy would decrease from $E = 7.6_{-0.7}^{+2.1} \cdot 10^{55} \text{ J}$ to $E = 6.4_{-0.6}^{+1.8} \cdot 10^{55} \text{ J}$,
620 and the minimum black hole mass gain from $\Delta M_{\bullet} > 8.5_{-0.8}^{+2.4} \cdot 10^8 M_{\odot}$ to $\Delta M_{\bullet} > 7.2_{-0.7}^{+2.0} \cdot 10^8 M_{\odot}$.

621 Finally, we arrive at a contradiction, as the quasar’s SMBH mass (measured from its SDSS BOSS spectrum)
622 $M_{\bullet} = 2.5 \pm 0.3 \cdot 10^8 M_{\odot}$ [49]. This mass is lower than the minimum mass gain associated to the fuelling of
623 Porphyrior’s jets. Thus, assuming that SDSS J152933.03+601552.5 is the outflow’s host galaxy leads to a contra-
624 diction. This argument reaffirms that J152932.16+601534.4 is Porphyrior’s host.

625 **Data availability** The LoTSS DR2 is publicly available at [https://lofar-surveys.org/dr2_release.](https://lofar-surveys.org/dr2_release.html)
626 [html](https://lofar-surveys.org/dr2_release.html). The authors will share this work’s proprietary LOFAR, uGMRT, and Keck I Telescope data, as well as
627 the dynamical model runs and LoTSS–VLASS spectral indices, upon reasonable request.

628 **Code availability** The dynamical model used to interpret the outflow is described by Hardcastle [2] and avail-
629 able for download at <https://github.com/mhardcastle/analytic>. Analysis and plotting code specific
630 to this work is available [50] on Code Ocean: <https://codeocean.com/capsule/3908804/tree>. There
631 are no access restrictions.

632 **Acknowledgments** M.S.S.L.O. and R.J.v.W. acknowledge support from the VIDI research programme with
633 project number 639.042.729, which is financed by the Dutch Research Council (NWO). M.S.S.L.O. also ac-
634 knowledges support from the CAS–NWO programme for radio astronomy with project number 629.001.024,
635 which is financed by the NWO. In addition, M.S.S.L.O., R.T., and R.J.v.W. acknowledge support from the
636 ERC Starting Grant ClusterWeb 804208. M.J.H. acknowledges support from the UK STFC [ST/V000624/1].
637 R.T. is grateful for support from the UKRI Future Leaders Fellowship (grant MR/T042842/1). A.B. acknowl-
638 edges financial support from the European Union - Next Generation EU. F.d.G. acknowledges support from
639 the ERC Consolidator Grant ULU 101086378. The work of D.S. was carried out at the Jet Propulsion Lab-
640 oratory, California Institute of Technology, under a contract with NASA. We thank Frits Sweijen for making
641 available `legacystamps` (<https://github.com/tikk3r/legacystamps>). We thank Riccardo Caniato
642 for illuminating discussions. LOFAR data products were provided by the LOFAR Surveys Key Science project
643 (LSKSP; <https://lofar-surveys.org/>) and were derived from observations with the International LO-
644 FAR Telescope (ILT). LOFAR [3] is the Low Frequency Array designed and constructed by ASTRON. It has
645 observing, data processing, and data storage facilities in several countries, which are owned by various parties
646 (each with their own funding sources), and which are collectively operated by the ILT foundation under a joint
647 scientific policy. The efforts of the LSKSP have benefited from funding from the European Research Council,
648 NOVA, NWO, CNRS-INSU, the SURF Co-operative, the UK Science and Technology Funding Council,
649 and the Jülich Supercomputing Centre. We thank the staff of the GMRT that made these observations possi-
650 ble. The GMRT is run by the National Centre for Radio Astrophysics of the Tata Institute of Fundamental
651 Research. Some of the data presented herein were obtained at the W. M. Keck Observatory, which is operated

652 as a scientific partnership among the California Institute of Technology, the University of California, and the
653 National Aeronautics and Space Administration. The Observatory was made possible by the generous financial
654 support of the W. M. Keck Foundation.

655 **Inclusion & ethics** We recognise that the Keck I Telescope observations on which this work relies have been
656 conducted from Maunakea, a site of high historical and religious significance in traditional Hawaiian culture.
657 We support deepening astronomy’s commitment to good stewardship of the mountain.

658 **Author contributions** A.R.D.J.G.I.B.G. and M.S.S.L.O. discovered Porphyrios; M.J.H., assisted by citizen
659 scientists, independently found the outflow as part of LOFAR Galaxy Zoo. M.S.S.L.O. coordinated the ensuing
660 project. R.J.v.W., H.J.A.R., and M.J.H. advised M.S.S.L.O. throughout. A.B. re-reduced and imaged the 6.2''
661 and 19.8'' LOFAR data; R.J.v.W. contributed. R.T. reduced and imaged the 0.4'' LOFAR data. F.d.G. explored
662 the use of LOFAR LBA data, which he reduced and imaged. M.S.S.L.O. wrote the uGMRT follow-up proposal.
663 M.S.S.L.O. and H.T.I. reduced and imaged the uGMRT data. S.G.D., D.S., and H.J.A.R. were instrumental
664 in securing Keck time (P.I.: S.G.D.). A.C.R. observed the host galaxy with LRIS; A.C.R. and D.S. reduced the
665 data. G.C.R. determined the host galaxy’s SED and stellar mass; M.S.S.L.O. contributed. M.J.H. determined
666 core spectral indices of Mpc-scale outflows. M.S.S.L.O. determined the spurious association probability, the
667 nearest galaxy cluster, and the circumgalactic Cosmic Web percentile. M.J.H. performed dynamical modelling;
668 M.S.S.L.O. contributed. M.S.S.L.O. derived the deprojection and filament heating formulae. M.S.S.L.O. wrote
669 the article, with contributions from A.R.D.J.G.I.B.G., R.T., and A.C.R. All authors provided comments to
670 improve the text.

671 **Author information** The authors declare no competing interests. Correspondence and requests for data
672 should be addressed to Martijn S.S.L. Oei, who can be reached via e-mail: oei@caltech.edu or
673 oei@strw.leidenuniv.nl.

674 References

- 675 1. Planck Collaboration *et al.* Planck 2018 results. VI. Cosmological parameters. *A&A* **641**, A6 (2020).
- 676 2. Hardcastle, M. J. A simulation-based analytic model of radio galaxies. *MNRAS* **475**, 2768–2786 (2018).
- 677 3. van Haarlem, M. P. *et al.* LOFAR: The LOw-Frequency ARray. *A&A* **556**, A2 (2013).
- 678 4. Shimwell, T. W. *et al.* The LOFAR Two-metre Sky Survey. V. Second data release. *A&A* **659**, A1 (2022).
- 679 5. Shimwell, T. W. *et al.* The LOFAR Two-metre Sky Survey. I. Survey description and preliminary data release. *A&A* **598**, A104
680 (2017).
- 681 6. Tasse, C. *et al.* *DDFacet: Facet-based radio imaging package* Astrophysics Source Code Library, record ascl:2305.008. 2023.
- 682 7. van Weeren, R. J. *et al.* LOFAR observations of galaxy clusters in HETDEX. Extraction and self-calibration of individual LO-
683 FAR targets. *A&A* **651**, A115 (2021).
- 684 8. Offringa, A. R. *et al.* WSCLEAN: an implementation of a fast, generic wide-field imager for radio astronomy. *MNRAS* **444**,
685 606–619 (2014).
- 686 9. Morabito, L. K. *et al.* Sub-arcsecond imaging with the International LOFAR Telescope. I. Foundational calibration strategy
687 and pipeline. *A&A* **658**, A1 (2022).
- 688 10. Jackson, N. *et al.* LBCS: The LOFAR Long-Baseline Calibrator Survey. *A&A* **595**, A86 (2016).
- 689 11. Jackson, N. *et al.* Sub-arcsecond imaging with the International LOFAR Telescope. II. Completion of the LOFAR Long-
690 Baseline Calibrator Survey. *A&A* **658**, A2 (2022).

- 691 12. Gupta, Y. *et al.* The upgraded GMRT: opening new windows on the radio Universe. *Current Science* **113**, 707–714 (2017).
- 692 13. Intema, H. T. *SPAM: Source Peeling and Atmospheric Modeling* Astrophysics Source Code Library, record ascl:1408.006. 2014.
- 693 14. Mohan, N. & Rafferty, D. *PyBDSF: Python Blob Detection and Source Finder* Astrophysics Source Code Library, record ascl:1502.007.
694 2015.
- 695 15. Blandford, R. D. & Znajek, R. L. Electromagnetic extraction of energy from Kerr black holes. *MNRAS* **179**, 433–456 (1977).
- 696 16. Hardcastle, M. J. *et al.* Radio-loud AGN in the first LoTSS data release. The lifetimes and environmental impact of jet-driven
697 sources. *A&A* **622**, A12 (2019).
- 698 17. Alam, S. *et al.* The Eleventh and Twelfth Data Releases of the Sloan Digital Sky Survey: Final Data from SDSS-III. *ApJS* **219**,
699 12 (2015).
- 700 18. Dey, A. *et al.* Overview of the DESI Legacy Imaging Surveys. *AJ* **157**, 168 (2019).
- 701 19. Duncan, K. J. All-purpose, all-sky photometric redshifts for the Legacy Imaging Surveys Data Release 8. *MNRAS* **512**, 3662–
702 3683 (2022).
- 703 20. Oke, J. B. *et al.* The Keck Low-Resolution Imaging Spectrometer. *PASP* **107**, 375 (1995).
- 704 21. McCarthy, J. K. *et al.* *Blue channel of the Keck low-resolution imaging spectrometer* in *Optical Astronomical Instrumentation* (ed
705 D’Odorico, S.) **3355** (1998), 81–92.
- 706 22. Steidel, C. C. *et al.* A Survey of Star-forming Galaxies in the $1.4 \lesssim z \lesssim 2.5$ Redshift Desert: Overview. *ApJ* **604**, 534–550
707 (2004).
- 708 23. Rockosi, C. *et al.* *The low-resolution imaging spectrograph red channel CCD upgrade: fully depleted, high-resistivity CCDs for*
709 *Keck in Ground-based and Airborne Instrumentation for Astronomy III* (eds McLean, I. S., Ramsay, S. K. & Takami, H.) **7735**
710 (2010), 77350R.
- 711 24. Prochaska, J. *et al.* PypeIt: The Python Spectroscopic Data Reduction Pipeline. *The Journal of Open Source Software* **5**, 2308
712 (2020).
- 713 25. Dawson, K. S. *et al.* The Baryon Oscillation Spectroscopic Survey of SDSS-III. *AJ* **145**, 10 (2013).
- 714 26. Chambers, K. C. *et al.* The Pan-STARRS_i Surveys. *arXiv e-prints*, arXiv:1612.05560 (2016).
- 715 27. Jarrett, T. H. *et al.* The Spitzer-WISE Survey of the Ecliptic Poles. *ApJ* **735**, 112 (2011).
- 716 28. Lang, D., Hogg, D. W. & Schlegel, D. J. WISE Photometry for 400 Million SDSS Sources. *AJ* **151**, 36 (2016).
- 717 29. Gordon, Y. A. *et al.* A Quick Look at the 3 GHz Radio Sky. I. Source Statistics from the Very Large Array Sky Survey. *ApJS* **255**,
718 30 (2021).
- 719 30. Helfand, D. J., White, R. L. & Becker, R. H. The Last of FIRST: The Final Catalog and Source Identifications. *ApJ* **801**, 26
720 (2015).
- 721 31. Calistro Rivera, G., Lusso, E., Hennawi, J. F. & Hogg, D. W. AGNfitter: A Bayesian MCMC Approach to Fitting Spectral
722 Energy Distributions of AGNs. *ApJ* **833**, 98 (2016).
- 723 32. Hardcastle, M. J. *et al.* The LOFAR Two-Metre Sky Survey. VI. Optical identifications for the second data release. *A&A* **678**,
724 A151 (2023).
- 725 33. Mostert, R. I. J. *et al.* Constraining the giant radio galaxy population with machine learning and Bayesian inference. *arXiv*
726 *e-prints*, arXiv:2405.00232 (2024).
- 727 34. Oei, M. S. S. L. *et al.* Luminous giants populate the dense Cosmic Web: The radio luminosity-environmental density relation
728 for radio galaxies in action. *arXiv e-prints*, arXiv:2404.17776 (2024).
- 729 35. Wen, Z. L. & Han, J. L. A catalog of 1.58 million clusters of galaxies identified from the DESI Legacy Imaging Surveys. *arXiv*
730 *e-prints*, arXiv:2404.02002 (2024).
- 731 36. Pasini, T. *et al.* Radio galaxies in galaxy groups: kinematics, scaling relations, and AGN feedback. *MNRAS* **505**, 2628–2637
732 (2021).
- 733 37. Arnaud, M. *et al.* The universal galaxy cluster pressure profile from a representative sample of nearby systems (REXCESS) and
734 the $Y_{SZ} - M_{500}$ relation. *A&A* **517**, A92 (2010).

- 735 38. Sun, M. *et al.* The Pressure Profiles of Hot Gas in Local Galaxy Groups. *ApJ* **727**, L49 (2011).
- 736 39. Cooke, R. J. & Fumagalli, M. Measurement of the primordial helium abundance from the intergalactic medium. *Nature As-*
737 *tronomy* **2**, 957–961 (2018).
- 738 40. Lovisari, L., Reiprich, T. H. & Schellenberger, G. Scaling properties of a complete X-ray selected galaxy group sample. *A&A*
739 **573**, A118 (2015).
- 740 41. Ricciardelli, E., Quilis, V. & Planelles, S. The structure of cosmic voids in a Λ CDM Universe. *MNRAS* **434**, 1192–1204 (2013).
- 741 42. Upton Sanderbeck, P. R., D’Aloisio, A. & McQuinn, M. J. Models of the thermal evolution of the intergalactic medium after
742 reionization. *MNRAS* **460**, 1885–1897 (2016).
- 743 43. Tuominen, T. *et al.* An EAGLE view of the missing baryons. *A&A* **646**, A156 (2021).
- 744 44. Oei, M. S. S. L. *et al.* Measuring the giant radio galaxy length distribution with the LoTSS. *A&A* **672**, A163 (2023).
- 745 45. Heckman, T. M. & Best, P. N. The Coevolution of Galaxies and Supermassive Black Holes: Insights from Surveys of the Con-
746 temporary Universe. *ARA&A* **52**, 589–660 (2014).
- 747 46. Correa, C. M. *et al.* Redshift-space effects in voids and their impact on cosmological tests. Part I: the void size function. *MNRAS*
748 **500**, 911–925 (2021).
- 749 47. Hardcastle, M. J. & Krause, M. G. H. Numerical modelling of the lobes of radio galaxies in cluster environments. *MNRAS*
750 **430**, 174–196 (2013).
- 751 48. Barrows, R. S., Comerford, J. M., Stern, D. & Assef, R. J. A Catalog of Host Galaxies for WISE-selected AGN: Connecting
752 Host Properties with Nuclear Activity and Identifying Contaminants. *ApJ* **922**, 179 (2021).
- 753 49. Chen, Z.-F., Pan, D.-S., Pang, T.-T. & Huang, Y. A Catalog of Quasar Properties from the Baryon Oscillation Spectroscopic
754 Survey. *ApJS* **234**, 16 (2018).
- 755 50. Oei, M. S. S. L. Code Ocean capsule for ‘Black hole jets on the scale of the Cosmic Web’. 2024.



Citation on deposit: Oei, M. S. S. L., Hardcastle, M. J., Timmerman, R., Gast, A. R. D. J. G. I. B., Botteon, A., Rodriguez, A. C., Stern, D., Calistro Rivera, G., van Weeren, R. J., Röttgering, H. J. A., Intema, H. T., de Gasperin, F., & Djorgovski, S. G. (2024). Black hole jets on the scale of the cosmic

web. *Nature*, 633(8030), 537-541. <https://doi.org/10.1038/s41586-024-07879-y>

For final citation and metadata, visit Durham Research Online URL:

<https://durham-repository.worktribe.com/output/2947816>

Copyright statement: This accepted manuscript is licensed under the Creative Commons Attribution 4.0 licence.

<https://creativecommons.org/licenses/by/4.0/>